Journal of Computational Physics 229 (2010) 594–625

Contents lists available at ScienceDirect

Journal of Computational Physics

journal homepage: www.elsevier.com/locate/jcp

Double-families of quasi-positive Darcy-flux approximations with highly anisotropic tensors on structured and unstructured grids

Michael G. Edwards *, Hongwen Zheng

Civil and Computational Engineering Centre, School of Engineering, Swansea University, Singleton Park Swansea, SA2 8PP Wales, UK

ARTICLE INFO

Article history:
Received 1 January 2009
Received in revised form 23 July 2009
Accepted 24 September 2009
Available online 4 October 2009

Keywords:
Double-family
Flux-continuous schemes
Locally conservative
Finite-volume
Control-volume distributed (CVD)
Multi-point flux approximation (MPFA)
Positivity
Monotonicity
Maximum principle
M-matrix
Full-pressure continuity
Anisotropy and pressure equation

ABSTRACT

This paper focuses on flux-continuous pressure equation approximation for strongly anisotropic media. Previous work on families of flux-continuous schemes for solving the general geometry–permeability tensor pressure equation has focused on single-parameter families. These schemes have been shown to remove the O(1) errors introduced by standard two-point flux reservoir simulation schemes when applied to full-tensor flow approximation. Improved convergence of the schemes has also been established for specific quadrature points. However these schemes have conditional M-matrices depending on the strength of the off-diagonal tensor coefficients. When applied to cases involving full-tensors arising from strongly anisotropic media, the point-wise continuous schemes can fail to satisfy the maximum principle and induce severe spurious oscillations in the numerical pressure solution.

New double-family flux-continuous locally conservative schemes are presented for the general geometry–permeability tensor pressure equation. The new double-family formulation is shown to expand on the current single-parameter range of existing conditional M-matrix schemes. The conditional M-matrix bounds on a double-family formulation are identified for both quadrilateral and triangle cell grids. A quasi-positive QM-matrix analysis is presented that classifies the behaviour of the new schemes with respect to double-family quadrature in regions beyond the M-matrix bounds. The extension to double-family quadrature is shown to be beneficial, resulting in novel optimal anisotropic quadrature schemes. The new methods are applied to strongly anisotropic full-tensor field problems and yield results with sharp resolution, with only minor or practically zero spurious oscillations.

1. Introduction

This paper presents the development of new double-families of flux-continuous finite-volume methods for the pressure equation resulting from Darcy's law and mass conservation. Key physical constraints of continuity in normal flux and full-pressure continuity are imposed at control-volume interfaces.

The derivation of algebraic flux continuity conditions for full-tensor discretization operators has lead to families of efficient locally conservative pointwise flux-continuous control-volume distributed (CVD) finite-volume schemes for determining the discrete pressure and velocity fields [1–5]. These schemes are constructed using linear triangular pressure support (TPS) inside each subcell for both quadrilateral and triangle grids, and are classified by the quadrature parameterization $0 < q \leqslant 1$. Schemes of this type are also called multi-point flux approximation schemes or MPFA [6] where focus has been on a scheme that is the default member of the above mentioned family with $q = 1$. Further schemes of this type are presented in [7,8] and via a novel mixed method [9]. Other schemes that preserve flux continuity have been developed from

* Corresponding author. Tel.: +44 1792 513175.
E-mail address: m.g.edwards@swansea.ac.uk (M.G. Edwards).

0021-9991/$ - see front matter © 2009 Elsevier Inc. All rights reserved.
doi:10.1016/j.jcp.2009.09.037

variational frameworks, using the mixed finite element method e.g. [10–15] and related work [16] and discontinuous galerkin methods [17,18], however these schemes require additional degrees of freedom.

When applying the flux-continuous schemes to the elliptic pressure equation with a strongly anisotropic full-tensor field they can fail to satisfy the maximum principle (as with other finite element and finite-volume methods) and result in spurious oscillations in the numerical pressure solution. M-matrix conditions were first derived in [19,1], monotone matrix conditions are presented in [20]. Grid optimization techniques have been proposed for improving stability of the discrete system for variable anisotropy [21]. Discretization schemes that help to improve stability for high anisotropy are presented in [4,22,23]. Non-linear methods have also been proposed, [24,25] (flux-splitting) and [26,27] (positivity preserving), both of which have been shown to yield numerical pressure solutions that are free of spurious oscillations.

In this paper new families of flux-continuous, locally conservative, finite-volume schemes are presented for solving the general-tensor pressure equation. The new schemes have full-pressure continuity imposed across control-volume faces, in contrast to the earlier families of flux-continuous schemes with pointwise continuity in pressure and flux. This work extends the single-parameter family of [22] to double-families of schemes on quadrilateral and triangular cell grids with general flexibility in quadrature that allow different quadrature points to be used on different control-volume subfaces.

For strongly anisotropic full-tensor cases where M-matrix conditions are violated, the earlier pointwise continuous families of schemes cannot avoid decoupling of the solution which leads to severe spurious oscillations in the discrete solution [22]. The new schemes minimiSe spurious oscillations in discrete pressure solutions. The new formulation leads to more robust quasi-positive families of flux-continuous schemes applicable to general discontinuous full-tensor fields. Particular focus is on two types of the many possible schemes within the formulation. The first involves identifying a family of optimal support schemes according to anisotropy, while the second involves extreme anisotropic quadrature schemes.

This paper is organized as follows: Section 2 gives a description of the single phase flow problem encountered in reservoir simulation with respect to the general-tensor pressure equation. Two-phase flow is also considered in the results section. The double-family of Full-Pressure Support (FPS) schemes is introduced in Section 3 for quadrilateral and triangular cell-vertex schemes. The relationship between FPS and control-volume finite element (CVFE) double-families is given in Section 4. Positivity is defined and double-family M-matrix conditions for quadrilateral schemes are derived in Section 5. Optimal and anisotropic quadrature schemes are introduced in Section 6, together with extreme anisotropic quadrature rules. Decoupled approximation, important consequences and implications for monotone schemes are presented in Section 7. Triangular grid M-matrix conditions are given in Section 8. Quasi-positive QM-matrices are defined in Section 9, where the double-family schemes are classified when M-matrix limits are exceeded. The cell-vertex FPS triangular grid formulation also leads to optimal schemes when anisotropy angle favoring triangulation is employed. Results for the new FPS schemes are presented in Section 10. Comparisons between the earlier TPS pointwise flux-continuous CVD(MPFA) schemes and new FPS schemes clearly demonstrate the benefits of the new schemes, both in terms of significantly reducing spurious oscillations and improving solution resolution. Conclusions follow in Section 11.

2. Flow equation and problem description

The analytical pressure equation is formulated in a general curvilinear coordinate system that is defined with respect to a uniform dimensionless transform space with a (ξ,η) coordinate system. (Neumann/Dirichlet) boundary conditions on boundary $\partial\Omega$. Choosing Ω to represent an arbitrary control-volume comprised of surfaces that are tangential to constant (ξ,η) respectively, where $\partial\Omega$ is the boundary of Ω and $\hat{n}$ is the unit outward normal. Spatial derivatives are expressed as $\phi_x = J(\phi,y)/J(x,y), \phi_y = J(x,\phi)/J(x,y)$ where $J(x,y) = x_\xi y_\eta - x_\eta y_\xi$ is the Jacobian. Resolving the x,y components of Darcy velocity $\mathbf{V} = -\mathbf{K}\nabla\phi$ along the unit normals to the curvilinear coordinates (ξ,η), e.g., normal to $\xi =$ constant, $\hat{\mathbf{n}}ds = (y_\eta, -x_\eta)d\eta$ gives rise to the general-tensor Darcy-flux components

$$F = -\int (T_{11}\phi_\xi + T_{12}\phi_\eta)\, d\eta, G = -\int (T_{12}\phi_\xi + T_{22}\phi_\eta)\, d\xi, \tag{1}$$

where general tensor $\mathbf{T} = |J|\mathbf{J}^{-1}\mathbf{K}\mathbf{J}^{-T}$ elements are given by

$$\begin{aligned} T_{11} &= \left(K_{11}y_\eta^2 + K_{22}x_\eta^2 - 2K_{12}x_\eta y_\eta\right)/J, \\ T_{22} &= \left(K_{11}y_\xi^2 + K_{22}x_\xi^2 - 2K_{12}x_\xi y_\xi\right)/J, \\ T_{12} &= \left(K_{12}(x_\xi y_\eta + x_\eta y_\xi) - (K_{11}y_\eta y_\xi + K_{22}x_\eta x_\xi)\right)/J \end{aligned} \tag{2}$$

and result from the Piola transformation. Matrix $\mathbf{K}$ is a diagonal or full elliptic cartesian tensor. The closed integral can be written as

$$\int\int_\Omega \frac{(\partial_\xi \widetilde{F} + \partial_\eta \widetilde{G})}{J} J d\xi d\eta = \triangle_\xi F + \triangle_\eta G = M \tag{3}$$

where $\triangle_\xi F$, $\triangle_\eta G$ are the differences in net flux with respect to ξ and η respectively, $\widetilde{F} = T_{11}\phi_\xi + T_{12}\phi_\eta$, and $\widetilde{G} = T_{12}\phi_\xi + T_{22}\phi_\eta$. M represents a specified flow rate. Ellipticity of $\mathbf{T}$ follows from that of K. full-tensors can arise from upscaling, unstructured grids and local orientation of the grid and permeability field.

3. Double-families of flux-continuous schemes with full-pressure support

Here we extend the single-parameter method of [22] to double-families of schemes which have continuous pressure support over the entirety of each control-volume subface. The double-families of schemes allow different quadrature points to be used on different control-volume subfaces leading to anisotropic quadrature schemes that prove to be beneficial for anisotropic problems.

Cell-vertex and cell-centred formulations are developed. In this section we present the cell-vertex quadrilateral grid formulation. The support and numbering for the cell-vertex scheme are shown in Fig. 1. A dual grid of polygonal control-volumes is constructed from the primal grid by joining primal grid cell-centres to cell-edge mid-points, so that each interior vertex is placed inside a control-volume Fig. 1(b). Discrete flow and rock variables are assigned to the grid vertices and permeability has a piecewise constant variation over the dual grid of control-volumes, Fig. 1(c). Introduction of the dual grid of control-volumes (dashed) partitions each primal grid cell into four sub-quadrilateral cells (subcells). Each subcell of a primal cell is therefore attached to a unique vertex and is also a subcell of the corresponding vertex control-volume. The subcell faces that lie inside a primal cell are thus subfaces of the corresponding vertex control-volumes and are interfaces across which permeability may jump in variation. Consequently the physical constraints of continuity in pressure and normal flux must be imposed across the resulting subfaces. This is achieved cell-wise, four local flux continuity conditions (together with pressure continuity) are imposed over the four interior subfaces between subcells in each primal cell to handle jumps in permeability between adjacent control-volumes. A further zero divergence constraint is also imposed in each primal cell to close the full pressure continuity system. The subface fluxes are then assembled over the vertex control-volumes to form the primal discrete approximation of Eq. (3), details are given below.

3.1. Double-families of full-pressure continuity schemes - quadrature parameterization

In this primal cell-vertex formulation, the continuity conditions are imposed locally in a cell-wise formulation. The *lowercase* indices (n, s, e, w) indicate the mid-points of the edges of a primal cell. The mid-points are connected to the primal cell centre m, forming the four interior subcell faces, or subfaces Fig. 2(a) where subfaces are indicated with dashed lines. Continuous interface pressures are introduced at the indicated fixed positions (n, s, e, w) in Fig. 2(a). Full subcell face pressure continuity is achieved by introduction of a further continuous interface pressure at the common corner m of the four subcells (i.e. at the primal cell centre) indicated in Figs. 1, and 2. The set of local interface pressures to be determined over the primal cell are thus defined by $\Phi_f = (\phi_n, \phi_s, \phi_e, \phi_w, \phi_m)^T$. The interface pressures are determined in terms of the four cell-vertex pressures in a pre-processing step, by four local flux continuity conditions (one per subface) and a zero divergence condition im-

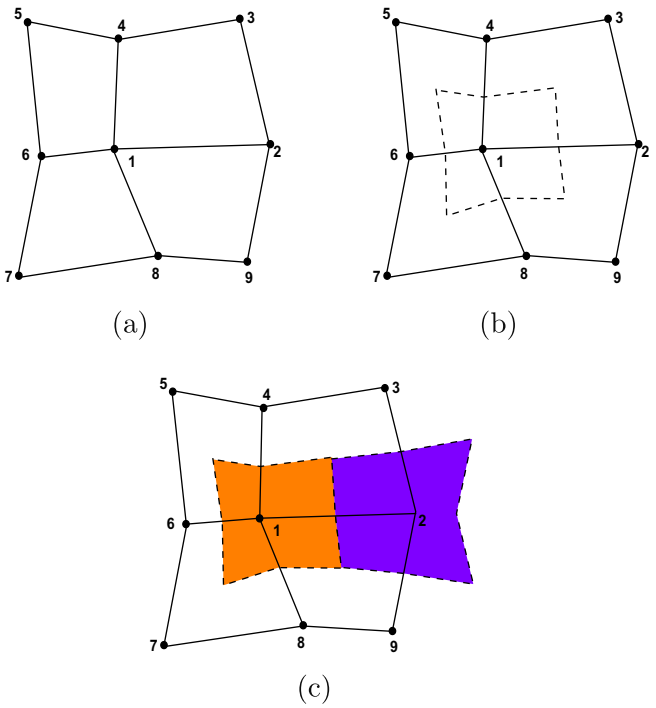

Fig. 1. (a) Numbering of scheme support nodes (stencil), (b) nine-node support, control-volume i, j dashed, with primal cell $i + 1/2, j + 1/2$ with local nodes 1–4, and (c) control-volumes with different rock properties shaded.

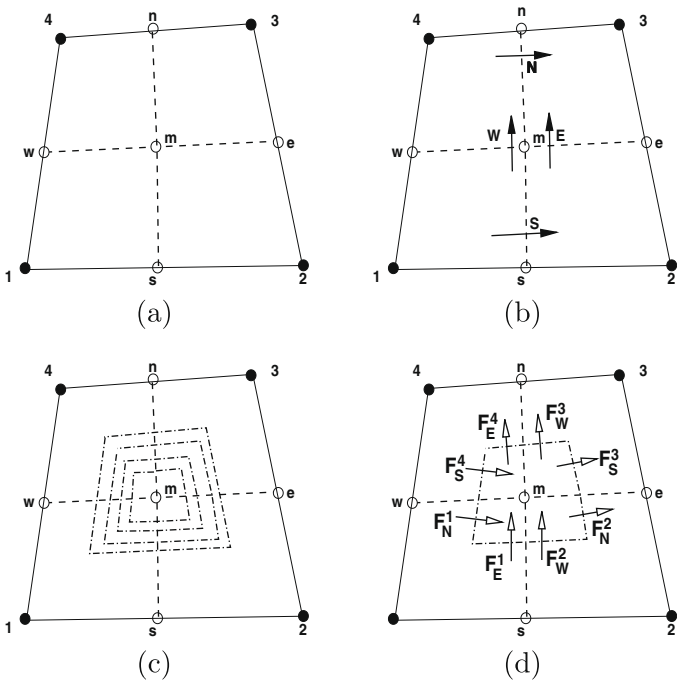

Fig. 2. (a) Primal cell nodes 1–4, interface nodes n, s, e, w, m, control-volume subfaces dashed, (b) double-family primary fluxes N, S, E, W in a cell (solid arrows), (c) auxiliary control-volumes (dot-dashed lines), and (d) auxiliary fluxes in a cell (hollow arrows).

posed over an auxiliary control-volume surrounding m inside the primal cell. Primary cell-vertex control-volume divergence is then obtained by cell-wise assembly of the resulting fluxes with respect to the primal vertex control-volumes.

A subcell bilinear approximation of pressure and position vector is introduced locally over each subcell with local (master element) parametric coordinates $(0 \leqslant \tilde{\xi}, \tilde{\eta} \leqslant 1)$ Fig. 3(a), where for example over subcell $(1, s, m, w)$ pressure and position vector are defined by

$$\phi = (1-\tilde{\xi})(1-\tilde{\eta})\phi_1 + \tilde{\xi}(1-\tilde{\eta})\phi_s + \tilde{\xi}\tilde{\eta}\phi_m + (1-\tilde{\xi})\tilde{\eta}\phi_w \tag{4}$$

$$\mathbf{r} = (1-\tilde{\xi})(1-\tilde{\eta})\mathbf{r}_1 + \tilde{\xi}(1-\tilde{\eta})\mathbf{r}_s + \tilde{\xi}\tilde{\eta}\mathbf{r}_m + (1-\tilde{\xi})\tilde{\eta}\mathbf{r}_w \tag{5}$$

The approximation leads to full-pressure support (FPS) over each subcell, in contrast to earlier triangle pressure support (TPS) schemes with pointwise interface pressure continuity. Consequently FPS has a conforming linear variation in pressure over each subcell face in a primal grid cell, which is shared by adjacent subcells with common subfaces, thus full-pressure continuity across interfaces follows by construction. The linear interface pressure variation permits a degree of freedom in position of flux continuity on each subface, leading to new families of flux-continuous schemes with full-pressure support. As a result of using bilinear basis functions the fluxes are consequently exact for any piecewise linear or bilinear pressure field provided the Darcy flux is continuous and consistently resolved in physical space as follows. Approximate derivatives are derived from the bilinear map over each subcell. For example over subcell 1 Fig. 2(a) with corners labeled anti-clockwise $(1, s, m, w)$, we obtain

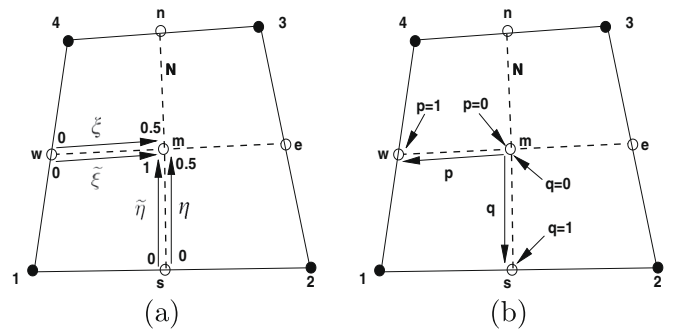

Fig. 3. Quadrature parameterization in a cell: (a) FPS $(\tilde{\xi}, \tilde{\eta})$ and CVFE (ξ, η), and (b) TPS (p, q).

$$\phi_{\tilde{\xi}} = (1-\tilde{\eta})(\phi_s - \phi_1) + \tilde{\eta}(\phi_m - \phi_w)$$
$$\phi_{\tilde{\eta}} = (1-\tilde{\xi})(\phi_w - \phi_1) + \tilde{\xi}(\phi_m - \phi_s) \tag{6}$$

with an analogous approximation for position vector derivatives.

$$\mathbf{r}_{\tilde{\xi}} = (1-\tilde{\eta})(\mathbf{r}_s - \mathbf{r}_1) + \tilde{\eta}(\mathbf{r}_m - \mathbf{r}_w)$$
$$\mathbf{r}_{\tilde{\eta}} = (1-\tilde{\xi})(\mathbf{r}_w - \mathbf{r}_1) + \tilde{\xi}(\mathbf{r}_m - \mathbf{r}_s) \tag{7}$$

Using Eqs. (6), (7) the discrete Darcy velocity at S is defined as

$$\mathbf{v}_h = -\mathbf{K}^1 \nabla \phi_h = -\mathbf{K}^1 \mathbf{G}(\tilde{\eta}) \begin{pmatrix} \phi_{\tilde{\xi}} \\ \phi_{\tilde{\eta}} \end{pmatrix} \tag{8}$$

where $\mathbf{K}^1$ is the local permeability tensor of vertex 1 and dependency of $\nabla\phi_h$ on quadrature point arises through

$$\nabla \phi_h = \mathbf{G}(\tilde{\eta}) \begin{pmatrix} \phi_{\tilde{\xi}} \\ \phi_{\tilde{\eta}} \end{pmatrix} = \begin{pmatrix} y_{\tilde{\eta}} & -y_{\tilde{\xi}} \\ -x_{\tilde{\eta}} & x_{\tilde{\xi}} \end{pmatrix} \frac{1}{J(x,y)} \begin{pmatrix} \phi_{\tilde{\xi}} \\ \phi_{\tilde{\eta}} \end{pmatrix} \tag{9}$$

Approximate $\mathbf{r}_{\tilde{\xi}}$ and $\mathbf{r}_{\tilde{\eta}}$ are defined by Eq. (7) and $J(x,y) = x_{\tilde{\xi}} y_{\tilde{\eta}} - x_{\tilde{\eta}} y_{\tilde{\xi}}$ over a subcell. The discrete normal Darcy flux at the left hand side of S Fig. 2(b), is then resolved along the outward normal vector $dL_S = ((y_m - y_s), -(x_m - x_s))$ and is expressed in terms of the resulting discrete general tensor $\mathbf{T} = \mathbf{T}(\tilde{\xi}, \tilde{\eta})$ as

$$F_S^1 = \mathbf{v}_h \cdot dL_S = -(T_{11}^1 \phi_{\tilde{\xi}} + T_{12}^1 \phi_{\tilde{\eta}})|_S^1 \tag{10}$$

where it is understood that the coefficients of $-(\phi_{\tilde{\xi}}, \phi_{\tilde{\eta}})|_S^1$ denoted by $T_{11}|_S^1$ and $T_{12}|_S^2$ are subcell (physical space) approximations of the general-tensor components (Eq. (10)) at the left hand face at S, which result from normal flux resolution. A similar expression for flux is obtained at the right-hand side of S from subcell 2 Fig. 2(b). The south flux is a function of $\tilde{\eta}$. Similarly subcell fluxes are resolved on the two sides of the other subfaces at E, W and N. Flux continuity is then imposed across the four cell interfaces at the four positions N, S, E, W Fig. 2(b) which are specified by chosen quadrature points. The E, W fluxes are defined with respect to $\tilde{\xi}$ and N, S fluxes are defined with respect to $\tilde{\eta}$.

Thus *upper-case* N, S, E, W define the primary flux positions of the family of schemes on the control-volume subfaces Fig. 2(b), where the fluxes have solid arrows. The actual interface pressures $(\phi_n, \phi_s, \phi_e, \phi_w)$ remain attached to the mid-points of the faces of the primal grid cell and m is fixed at the primal cell centre. The complete vector of interface pressures $\Phi_f = (\phi_n, \phi_s, \phi_e, \phi_w, \phi_m)^T$ are expressed in terms of the primal pressure degrees of freedom $\Phi_v = (\phi_1, \phi_2, \phi_3, \phi_4)^T$ at the vertices of the primal cell prior to the solution step, by imposing flux continuity across the four subcell faces inside the cell, together with a local zero divergence condition for ϕ_m.

The primal cell divergence approximation is introduced over an auxiliary control-volume surrounding the cell centre. The location of the auxiliary control-volume is another parameter to be specified, e.g. any of the indicated dot-dashed lines in Fig. 2(c) and (d). The four flux continuity conditions together with the zero divergence condition lead to the local algebraic system

$$\begin{aligned}
&F_N = -(T_{11}\phi_{\tilde{\xi}} + T_{12}\phi_{\tilde{\eta}})|_N^3 = -(T_{11}\phi_{\tilde{\xi}} + T_{12}\phi_{\tilde{\eta}})|_N^4,\\
&F_S = -(T_{11}\phi_{\tilde{\xi}} + T_{12}\phi_{\tilde{\eta}})|_S^1 = -(T_{11}\phi_{\tilde{\xi}} + T_{12}\phi_{\tilde{\eta}})|_S^2,\\
&F_E = -(T_{12}\phi_{\tilde{\xi}} + T_{22}\phi_{\tilde{\eta}})|_E^2 = -(T_{12}\phi_{\tilde{\xi}} + T_{22}\phi_{\tilde{\eta}})|_E^3,\\
&F_W = -(T_{12}\phi_{\tilde{\xi}} + T_{22}\phi_{\tilde{\eta}})|_W^1 = -(T_{12}\phi_{\tilde{\xi}} + T_{22}\phi_{\tilde{\eta}})|_W^4,\\
&-\sum_{\partial\Omega_{AUX}} (\mathbf{K}\nabla\phi)\cdot\hat{\mathbf{n}}\Delta s = 0
\end{aligned} \tag{11}$$

which is linear in Φ_f and Φ_v. The double-family of schemes is defined by the positions of flux continuity parameterized by the local basis function $\tilde{\xi}, \tilde{\eta}$, with respect to pairs of subcell faces. The double-parameter family is distinguished from a single-parameter family by allowing quadrature points that are not necessarily equal along adjoining subcell faces so that $\tilde{\xi} \neq \tilde{\eta}$. This will lead to anisotropic quadratures defined later.

To clarify notation, for example F_S will denote the continuous flux at a quadrature point that may either coincide with s or be between s and m, but never coincides with m, i.e. $0 \leqslant \tilde{\eta} < 1$. Following a standard finite-volume procedure, the flux is added to the control-volume with local number 1 and subtracted from adjacent control-volume 2 in the cell-wise assembly process. Local conservation follows immediately since the net sum of flux leaving and entering the two control-volumes sharing the common subface is zero. Similarly F_W denotes the flux at a quadrature point between w and m, but never coincides with m, i.e. $0 \leqslant \tilde{\xi} < 1$. This flux is added to control-volume 1 and subtracted from adjacent control-volume 4. Thus local conservation is strictly enforced on a subface basis for any quadrature point, which applies to any grid type.

However, one of the distinguishing features of this finite-volume scheme is the local imposition of in-built flux continuity across interfaces separating medium variation for general anisotropic quadrature. Here we illustrate discrete flux continuity for the second and fourth equations of Eq. (11), which are defined by different values of $\tilde{\xi}$ and $\tilde{\eta}$ respectively. The second equation is defined at a point S between s and m with

$$F_S = -(T^1_{11}((1-\tilde{\eta})(\phi_s-\phi_1)+\tilde{\eta}(\phi_m-\phi_w))+T^1_{12}(\phi_m-\phi_s))$$
$$= -(T^2_{11}((1-\tilde{\eta})(\phi_2-\phi_s)+\tilde{\eta}(\phi_e-\phi_m))+T^2_{12}(\phi_m-\phi_s)) \quad (12)$$

where for the left hand side flux, approximations of $\phi_{\tilde{\xi}}$ and $\phi_{\tilde{\eta}}$ are given by Eq. (6) and F_S is a function of $\tilde{\eta}$, $F_S = F_S(\tilde{\eta})$ and the geometric tensor coefficients are calculated at S where the position is defined by the quadrature point $\tilde{\eta}$, where $\mathbf{r}|_S = (1-\tilde{\eta})\mathbf{r}_s + \tilde{\eta}\mathbf{r}_m$.

The fourth equation is defined at a point W between w and m (again never coinciding with m) with

$$F_W = -\left(T^1_{12}(\phi_m-\phi_w)+T^1_{22}((1-\tilde{\xi})(\phi_w-\phi_1)+\tilde{\xi}(\phi_m-\phi_s))\right)$$
$$= -\left(T^4_{12}(\phi_m-\phi_w)+T^4_{22}((1-\tilde{\xi})(\phi_4-\phi_w)+\tilde{\xi}(\phi_n-\phi_m))\right) \quad (13)$$

where for the left hand side flux (with respect to edge (m,w)), approximations of $\phi_{\tilde{\xi}}$ and $\phi_{\tilde{\eta}}$ are again given by Eq. (6) and now F_W is a function of $\tilde{\xi}$, $F_W = F_W(\tilde{\xi})$ and the tensor coefficients are calculated at W where the position is defined by the quadrature point $\tilde{\xi}$, $\mathbf{r}|_W = (1-\tilde{\xi})\mathbf{r}_w + \tilde{\xi}\mathbf{r}_m$.

Analogous subcell approximations are constructed for each of the flux continuity conditions in Eq. (11), leading to $F_N(\tilde{\eta}), F_S(\tilde{\eta}), F_E(\tilde{\xi}), F_W(\tilde{\xi})$ which are not necessarily symmetrically located c.f. Fig. 2(b), where $\tilde{\xi} \neq \tilde{\eta}$ creating double-families. The actual choice of quadrature points $(\tilde{\xi},\tilde{\eta})$ are discussed in Section 6.

Referring now to the discrete auxiliary divergence approximation, the 5th equation of Eq. (11), the auxiliary control-volume (perimeter shown dot-dashed) centred on the auxiliary node m of Fig. 2(c) and (d) is comprised of 4 *sub-subcells* one in each subcell of the primal cell, where permeability is piecewise constant, so the auxiliary divergence approximation is based on a CVFE formulation. The auxiliary fluxes are also parameterized with respect to $0 \leqslant p < 1$ defined over the auxiliary control-volume subfaces. The auxiliary control-volume can lie in or on the primal cell, the size is to be chosen, and parameterized by the variable $1 \geqslant c > 0$, where $c = 1$ corresponds to an auxiliary control-volume that overlays the primal cell and as $c \to 0$ the auxiliary control-volume tends to zero. A small volume maximises primal flux quadrature range c.f. Section 4 below.

The primal control-volume and auxiliary control-volume fluxes are indicated in Fig. 2(b) and (d), respectively, with solid arrows for primal fluxes and hollow arrows for auxiliary fluxes. The auxiliary fluxes are defined with tensors T and have super-fixes indicating the auxiliary subcell and compass suffices indicating position relative to the primal subcell in which they are defined. For example referring again to subcell 1 (corners $1, s, m, w$) Fig. 2(d), the auxiliary control-volume flux F^1_N is defined on the top left sub-subcell face by

$$F^1_N = c(-\mathsf{T}^1_{11}(c(1-p)(\phi_s-\phi_1)+(1-c(1-p))(\phi_m-\phi_w))-\mathsf{T}^1_{12}(c(\phi_w-\phi_1)+(1-c)(\phi_m-\phi_s))) \quad (14)$$

which is a function of the auxiliary quadrature and control-volume size parameters p and c respectively. In the general case this formulation leads to a multiple family of schemes which are functions of the primary flux quadrature parameters $\tilde{\xi},\tilde{\eta}$, the auxiliary control-volume flux parameter p and auxiliary control-volume size parameter c.

The degrees of freedom of the five equation system Eq. (11) are the five interface pressures $\Phi_f = (\phi_n,\phi_s,\phi_e,\phi_w,\phi_m)^T$ and the four cell-vertex pressures $\Phi_v = (\phi_1,\phi_2,\phi_3,\phi_4)^T$. The system of equations is rearranged as

$$\mathbf{F} = A^{5\times5}_L \Phi_f + B^{5\times4}_L \Phi_v = A^{5\times5}_R \Phi_f + B^{5\times4}_R \Phi_v \quad (15)$$

where $A^{5\times5}_L, A^{5\times5}_R$ are 5×5 matrices and $B^{5\times4}_L, B^{5\times4}_R$ 5×4 matrices. Since we only require the four fluxes, we let $A^{4\times5}_L$ denote the first four rows of matrix $A^{5\times5}_L$ and $B^{4\times4}_L$ denote the first four rows of matrix $B^{5\times4}_L$.

Then the continuous fluxes of the families of FPS schemes are written as:

$$\mathbf{F} = \left(A^{4\times5}_L (A^{5\times5}_L - A^{5\times5}_R)^{-1}(B^{5\times4}_R - B^{5\times4}_L) + B^{4\times4}_L\right)\Phi_v \quad (16)$$

where $\mathbf{F} = (F_N, F_S, F_E, F_W)^T$. Fluxes are then assembled from respective grid cells to form control-volume face flux approximations. This formulation applies to a general quadrilateral cell belonging to any grid type. Using flux consistency [28], the fluxes of Eq. (16) can be written as $A\mathbf{F} = -\Delta\Phi_v$ denoting a linear combination of local cell-edge pressure differences, where A is the local flux matrix.

For a structured grid the net flux across the right-hand face of control-volume i,j (local node 1) is given by $F_{i+1/2,j} = F_{S_{i+1/2,j+1/2}} + F_{N_{i+1/2,j-1/2}}$, which depends on the six vertices 8, 9, 1, 2, 3, 4 and the net flux across the upper face of control-volume i,j is given by $F_{ij+1/2} = F_{E_{i-1/2,j+1/2}} + F_{W_{i+1/2,j+1/2}}$ which depends on the six vertices 6, 1, 2, 3, 4, 5 and where $i+1/2, j+1/2$ are integer coordinates of the top right-hand grid cell, local nodes 1–4 Fig. 1(b). The discrete divergence

$$F_{i+1/2,j} - F_{i-1/2,j} + F_{i,j+1/2} - F_{i,j-1/2} = M_{i,j}$$

is then formed over each control-volume via cell-wise assembly.

3.2. FPS schemes on triangle grids

The generalisation of the cell-vertex method to triangles follows a similar procedure to the above method for quadrilaterals. Primary pressure variables are located at the primal grid cell-vertices as for the quadrilateral case above, with primary variable pressures locally numbered with respect to the triangle vertices viz $\Phi_v = (\phi_1, \phi_2, \phi_3)^T$ with suffix v for vertices, as indicated in Fig. 4. There are now three subcells meeting inside the triangle, formed by joining triangle edge mid-points n, s, e with the triangle centre or circumcentre m, Fig. 4(a). Each subcell belongs to a unique vertex of the triangle. A control-volume surrounding a given vertex is comprised of all subcells attached to the vertex Fig. 4(b). Rock properties are assigned to the control-volumes over which permeability is then piecewise constant, shown shaded in Fig. 4(c). The local flux continuity conditions are again naturally imposed via a primal cell-wise formulation. Continuous interface pressures are introduced at

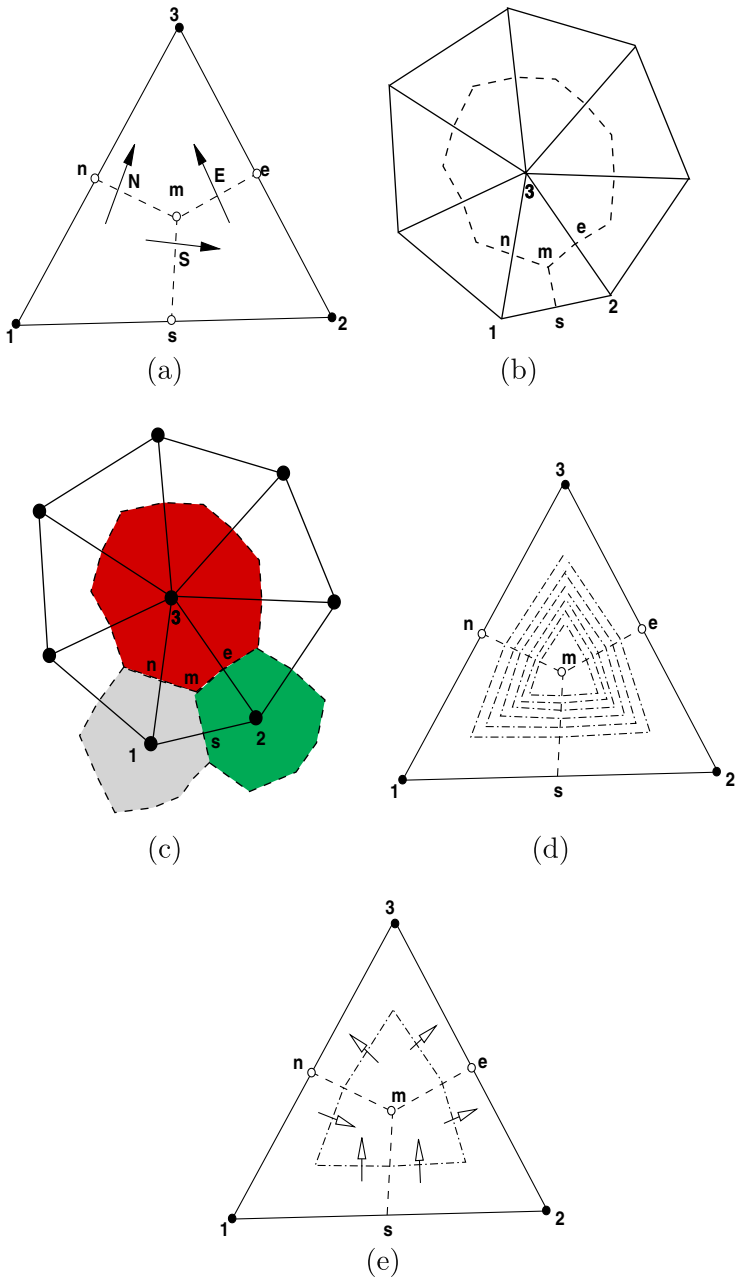

Fig. 4. (a) Primal fluxes in triangle (solid arrows) on control-volume subcell faces (dashed), (b) primal control-volume (dashed) surrounding node 3, (c) control-volumes with different rock properties shaded, (d) auxiliary control-volumes in triangle (dot-dashed lines), and (e) auxiliary fluxes in a triangle (hollow arrows).

the triangle edge mid-points and centre respectively, where the subcells meet. Thus the vector of auxiliary interface pressures is defined by $\Phi_f = (\phi_n, \phi_s, \phi_e, \phi_m)^T$. A local bilinear variation in pressure is introduced over each subcell as before. Adjacent interior subcell faces share the same conforming linear pressure variation on each common subface, ensuring full interface pressure continuity by construction. One flux continuity condition is imposed on each of the three subcell faces (dashed subfaces Fig. 4(a) to determine ϕ_n, ϕ_s, ϕ_e, where a distinct quadrature can be employed on each subface, leading to double-family fluxes $\mathbf{F} = (F_N, F_S, F_E)^T$. Zero divergence is applied over a small auxiliary control-volume (dot-dashed) surrounding the triangle centre of gravity Fig. 4(d) and (e), to determine ϕ_m, providing a total of four equations for the four auxiliary interface pressures Φ_f. The resulting system of equations are given by

$$\begin{aligned} F_N &= -(T_{11}\phi_{\tilde{\xi}} + T_{12}\phi_{\tilde{\eta}})|_N^3 = -(T_{12}\phi_{\tilde{\xi}} + T_{22}\phi_{\tilde{\eta}})|_N^1, \\ F_S &= -(T_{11}\phi_{\tilde{\xi}} + T_{12}\phi_{\tilde{\eta}})|_S^1 = -(T_{11}\phi_{\tilde{\xi}} + T_{12}\phi_{\tilde{\eta}})|_S^2, \\ F_E &= -(T_{12}\phi_{\tilde{\xi}} + T_{22}\phi_{\tilde{\eta}})|_E^2 = -(T_{12}\phi_{\tilde{\xi}} + T_{22}\phi_{\tilde{\eta}})|_E^3, \\ &- \sum_{\partial\Omega_{AUX}} (\mathbf{K}\nabla\phi)\cdot\hat{\mathbf{n}}\Delta s = 0 \end{aligned} \tag{17}$$

which is linear in Φ_f and Φ_v, and represents the triangle grid equivalent of Eq. (11). Again discrete approximations of the general-tensor coefficients result from normal Darcy-flux resolution over the interior subcell faces. Approximation of Eq. (17) and subsequent elimination of the auxiliary pressures follows an analogous procedure to that of Eqs. (12)–(16), where now we obtain

$$\mathbf{F} = \left(A_L^{3\times4}(A_L^{4\times4} - A_R^{4\times4})^{-1}(B_R^{4\times3} - B_L^{4\times3}) + B_L^{3\times3}\right)\Phi_v \tag{18}$$

Primal divergence is then approximated by assembly of the continuous control-volume subcell fluxes over each polygon surrounding each vertex. For example flux F_S is added to control-volume 1 and subtracted from adjacent control-volume 2 for any quadrature point between s and m but not at m, Fig. 4. Local conservation follows immediately as the two flux contributions cancel in the summation of the divergence contributions from subface $s-m$ to vertices 1 and 2 respectively. Finally we note that as for quadrilateral cell fluxes, triangle cell fluxes of Eq. (18) can also be written as a linear combination of cell-edge differences in pressure by using the flux consistency condition [28].

4. Double-family relationship between FPS and CVFE for a spatially constant tensor

Flux continuity ensures local conservation, however the converse is not necessarily true, for example the CVFE family is locally conservative [19], but key flux continuity is lacking across the interior interfaces where permeability can be discontinuous. Thus standard CVFE methods are not appropriate for modeling flow in porous media.

However, for a spatially constant tensor field the quadrilateral flux-continuous schemes are mapped onto the more transparent control-volume finite element CVFE nine-point framework. This relationship aids understanding of TPS and FPS discretization effects, see [1,22] for the single family FPS analysis. Here $0 \leqslant \xi, \eta \leqslant 1$ define master element coordinates over the primal cell if cell-vertex, or dual-cell if cell centred. Bilinear expansions of $\phi, \mathbf{r}$ in ξ, η are used in defining the CVFE double-family over the primal cell or the dual-cell, Fig. 1(b), where e.g.

$$\phi = (1-\xi)(1-\eta)\phi_1 + \xi(1-\eta)\phi_2 + \xi\eta\phi_3 + (1-\xi)\eta\phi_4 \tag{19}$$

Derivatives of the bilinear expansions of $\phi, \mathbf{r}$ in ξ, η are then used in defining the CVFE double-family fluxes over the primal cell (dual-cell if cell-centred), Fig. 1(b). The resulting fluxes at S and W contributing to control-volume 1 are given by

$$\begin{aligned} F_S &= -\tfrac{1}{2}(T_{11}((\phi_2-\phi_1)(1-\eta) + (\phi_3-\phi_4)\eta) + \tfrac{1}{2}T_{12}((\phi_4-\phi_1) + (\phi_3-\phi_2))) \\ F_W &= -\tfrac{1}{2}(\tfrac{1}{2}T_{12}((\phi_2-\phi_1) + (\phi_3-\phi_4)) + T_{22}((\phi_4-\phi_1)(1-\xi) + (\phi_3-\phi_2)\xi)) \end{aligned} \tag{20}$$

where $0 \leqslant \xi, \eta < 1/2$ Fig. 3(a), ensuring that flux approximation remains convex over the control-volume and that the quadrature points do not both coincide with the decoupled point $\xi = \eta = 1/2$ at the cell centre (discussed later). Crucially here these double-family schemes also permit quadratures with $\xi \neq \eta$. The nine-point scheme coefficients for the case of a spatially constant full-tensor are given below.

Note $0 \leqslant \xi, \eta < 1/2$ for fluxes defined in their respective control-volumes. The CVFE double-family framework is a natural extension of the single family [19] and is quite transparent and includes all possible double-parameter, consistent, locally conservative, nine-point diagonal and full-tensor schemes, for spatially constant tensor coefficients. By construction c.f. Eqs. (19) and (20), for spatially constant tensor coefficients the CVFE fluxes and schemes are exact for linear and bilinear solutions of the respective pressure equations defined in Appendix A.

Symmetry of the double-family for constant coefficients is verified by inspection of Table 1. The CVFE family is symmetric positive definite [22,19] and the double-family is SPD, by a similar proof. From the mapping below it follows that the FPS families of schemes are therefore SPD for spatially constant elliptic tensor coefficients for $0 \leqslant \xi, \eta < 1/2$.

4.1. Full-pressure support FPS and CVFE mapping

For a spatially constant tensor the FPS schemes can also be expressed in the form of Table 1 with ξ, η in the CVFE scheme defined by

$$\begin{aligned} \xi &= \tfrac{1}{2}(\tilde{\xi} + t(\tilde{\xi}, \tilde{\eta})ER) \\ \eta &= \tfrac{1}{2}(\tilde{\eta} + t(\tilde{\xi}, \tilde{\eta})ER) \end{aligned} \tag{21}$$

where

$$t(\tilde{\xi}, \tilde{\eta}) = \frac{c(2 - \tilde{\xi} - \tilde{\eta})(T_{11} + T_{22})}{(1+c)((1-\tilde{\eta})T_{11} + (1-\tilde{\xi})T_{22}) + c(T_{11} + T_{22})} \tag{22}$$

where $R = \frac{4T_{11}T_{22}}{(T_{11}+T_{22})^2}$ (harmonic/arithmetic means), and $E = \frac{T12^2}{T_{11}T_{22}}$ (ellipticity measure) where $R, E \leqslant 1$, and $0 \leqslant \eta < 1/2$, with maximum quadrature bounded above by 1/2. The lower bounds of ξ, η only tend to zero if the auxiliary control-volume size tends to zero (by Eq. (22)), which occurs in the limit with $c \to 0$, and from Eq. (21) it follows that $\xi = \tilde{\xi}/2, \eta = \tilde{\eta}/2$ and the FPS flux integration intervals map onto the CVFE intervals with $0 \leqslant \xi, \eta < \frac{1}{2}$, Fig. 3(a). Therefore an M-matrix analysis of the CVFE double-family with coefficients in Table 1 is applicable to the FPS double-family.

4.2. Triangular Pressure Support TPS and CVFE Mapping

The original pointwise continuous schemes with triangle pressure support (TPS) also extend to a double-family with nine-point coefficients given by Table 1 and corresponding mapping

$$\xi = \frac{(pE + q - pq)}{2(p + q - pq)}, \quad \eta = \frac{(p + qE - pq)}{2(p + q - pq)} \tag{23}$$

where E is defined above and $0 < p, q \leqslant 1$ are local quadrature coordinates measured from the cell centre to the cell-face mid-points Fig. 3(b), [1]. This shows that an M-matrix analysis of the CVFE double-family applies to the TPS double-family. However as for the original single-parameter family, for high full-tensor anisotropy ratio where $E \to 1$, from Eq. (23) it follows that $\xi \to 1/2$ and $\eta \to 1/2$ leading to a decoupled formulation, discussed further below.

5. Positivity, M-matrix and discrete maximum principle

The term monotonicity is too strong when describing multi-dimensional solutions, as the local solution can often have a saddle point in structure [22], where as a result positivity is introduced. We recall these definitions below.

5.1. Local saddle point nature of elliptic solutions

Consider a locally constant tensor field away from any source/sink, where the pressure equation reduces to $-\widetilde{K}_{11}\phi_{\tilde{x}\tilde{x}} - \widetilde{K}_{22}\phi_{\tilde{y}\tilde{y}} = 0$ with respect to principal axes $(\tilde{x}, \tilde{y})$, so that $\phi_{\tilde{x}\tilde{x}} = -\widetilde{K}_{22}\phi_{\tilde{y}\tilde{y}}/\widetilde{K}_{11}$, from which it follows that $\phi_{\tilde{x}\tilde{x}}\phi_{\tilde{y}\tilde{y}} < 0$ leading to the condition for a saddle point with $\phi^2_{\tilde{x}\tilde{y}} \geqslant \phi_{\tilde{x}\tilde{x}}\phi_{\tilde{y}\tilde{y}}$. Consequently we use the term positive as defined below for describing the property of a scheme that ensures discrete solutions are computed that are free of spurious oscillations. This name has been taken from the hyperbolic scheme literature [30] and the definition below has a direct analogy.

5.2. Definition of a positive elliptic scheme

Well known conditions for a matrix A with elements $a_{i,j}$ to be an M-matrix are that the diagonal coefficients be positive $a_{i,i} > 0$ and the matrix be strictly diagonally dominant or weakly diagonally dominant with strict inequality for at least one row, **A** must also be irreducible and $a_{i,j} \leqslant 0, i \neq j$. For the ith equation it follows that away from a source or sink

Table 1
CVFE double-family coefficients for constant tensor field.

Integer coordinates	Coefficients	Full-tensor
i,j	M11	$2(T_{11} + T_{22}) - 2(\eta T_{11} + \xi T_{22})$
$i+1,j$	M12	$-T_{11} + (\eta T_{11} + \xi T_{22})$
$i+1,j+1$	M13	$-\frac{1}{2}(\eta T_{11} + \xi T_{22}) - \frac{1}{2}T12$
$i,j+1$	M14	$-T_{22} + (\eta T_{11} + \xi T_{22})$
$i-1,j+1$	M15	$-\frac{1}{2}(\eta T_{11} + \xi T_{22}) + \frac{1}{2}T12$
$i-1,j$	M16	$-T_{11} + (\eta T_{11} + \xi T_{22})$
$i-1,j-1$	M17	$-\frac{1}{2}(\eta T_{11} + \xi T_{22}) - \frac{1}{2}T12$
$i,j-1$	M18	$-T_{22} + (\eta T_{11} + \xi T_{22})$
$i+1,j-1$	M19	$-\frac{1}{2}(\eta T_{11} + \xi T_{22}) + \frac{1}{2}T12$

$$\phi_i = -\frac{1}{a_{ii}} \sum_{j(i \neq j)} a_{ij}\phi_j \tag{24}$$

If **A** is an M-matrix, by consistency for a constant potential field it follows from Eq. (24) that each non-specified ϕ_i is a convex average of the surrounding nodes or neighbours, belonging to the discretization support centred on node *i*. Thus each ϕ_i is bounded between the maximum and minimum of the neighbours with

$$\phi_{imin} \leqslant \phi_i \leqslant \phi_{imax} \tag{25}$$

where ϕ_{imax}, ϕ_{imin} are the respective maximum and minimum values of pressure at the neighbouring nodes belonging to the support at node *i*. This condition is consistent with the absence of spurious oscillations and defines a local discrete maximum principle (DMP). Thus when **A** is an M-matrix Eq. (24) defines a positive scheme.

5.3. Quadrilateral M-matrix conditions and cell-wise analysis

An M-matrix analysis of FPS is conducted by considering cell-wise assembly of fluxes for the cell-vertex formulation and dual-cell assembly of fluxes for the cell-centred formulation [1,19,22]. The following analysis relies on the assumption that the tensor is piecewise constant over the grid cells for the cell-vertex formulation (and piecewise constant over the dual-cell for the cell-centred formulation). Assumption of a piecewise constant tensor per grid cell is standard for CVFE and thus the cell-wise M-matrix analysis below applies directly to the discrete CVFE method. For a variable or heterogeneous permeability field where for FPS, permeability changes between the respective control-volume subcells belonging to the grid cell, this assumption then applies to the locally upscaled (homogenized) general tensor over the grid cell, so that the resulting conditions hold with respect to the resulting local cell average tensor. However, the general FPS flux for discontinuous coefficients can also be written as a linear combination of cell-edge differences (by using flux consistency [28]) and a similar analysis treating the non-symmetric case applies.

Here we perform a primal cell-wise M-matrix test for the cell-vertex double-family, where e.g. for local node 1, the local net flux contribution to the global matrix is given by $F_S + F_W$ Fig. 2(b).

Using Eq. (20) and gathering coefficients of each $\phi_j, j = 1, \ldots, 4$ the net flux is written as

$$F_S + F_W = \frac{1}{2}(\phi_1(T_{11}(1-\eta) + T_{22}(1-\xi) + T_{12}) - \phi_2(T_{11}(1-\eta) - T_{22}\xi) - \phi_3(T_{11}\eta + T_{22}\xi + T_{12}) - \phi_4(T_{22}(1-\xi) - T_{11}\eta)) \tag{26}$$

Next the conditions for diagonal dominance with non-positive off diagonals are tested, where the diagonal corresponds to local node 1. First conditions for non-positive off-diagonal coefficients are derived. The ϕ_3 coefficient is non-positive if

$$|T_{12}| \leqslant (T_{11}\eta + T_{22}\xi) \tag{27}$$

and the coefficients of ϕ_2 and ϕ_4 are non-positive if

$$(\eta T_{11} + \xi T_{22}) \leqslant min(T_{11}, T_{22}) \tag{28}$$

Thus taking the inequalities together we obtain

$$|T_{12}| \leqslant (\eta T_{11} + \xi T_{22}) \leqslant min(T_{11}, T_{22}) \tag{29}$$

from which it follows that diagonal dominance is obtained with the coefficient of ϕ_1 positive and equal to the sum of absolute values of the off-diagonal coefficients, with strict inequality obtained when a Dirichlet condition is imposed. Here ξ, η can be defined independently leading to a wide range of double-family flux quadrature points. We note that M-matrix conditions for the single family of schemes are recovered for $\xi = \eta$ in Eq. (29) [1].

The double-family nine-node M-matrix conditions of Eq. (29) can also be verified by inspection of Table 1. One of the essential conditions here is that

$$|T_{12}| \leqslant min(T_{11}, T_{22}) \tag{30}$$

which is only *sufficient for ellipticity* $\left(T_{12}^2 \leqslant T_{11}T_{22}\right)$ as for single family schemes [22]. Thus elliptic tensors with $|T_{12}| > min(T_{11}, T_{22})$ violate the M-Matrix criteria of Eq. (29) and expose the upper M-Matrix limit.

These conditions now establish the following Conditional M-matrix theorem: *Any double-parameter family of consistent locally conservative schemes on or within the nine-point stencil applied to a the pressure equation with a spatially constant full-tensor field can only provide a conditional M-matrix subject to Eq. (29).* Note: FPS fluxes are exact for piecewise linear and bilinear fields since the pressure basis functions are piecewise bilinear, c.f. Eq. (5). In these cases FPS schemes are exact as defined in Appendix A. For a spatially constant full-tensor field the FPS schemes then reduce to the schemes in the theorem, which are exact for linear and bilinear fields as discussed earlier c.f. Section 4.

6. Anisotropic quadrature and optimal support

In this section two particular approaches are proposed for designing schemes using quadrature rules that will yield solutions with improved resolution for full-tensor fields. The first involves optimal support schemes, while the second involves extreme anisotropic quadrature. Schemes for large grid aspect ratio and/or large anisotropy ratio with small or zero off-diagonal coefficients are also presented.

First we develop a family of optimal support schemes. If we choose quadrature points ξ, η such that

$$\eta T_{11} + \xi T_{22} = |T_{12}| \tag{31}$$

then an M-matrix is obtained subject to the sufficient condition for ellipticity of Eq. (30), giving the maximum upper limit on the tensor cross-term. Thus Eq. (31) generalises the result of [1] where $\xi = \eta = |T_{12}|/(T_{11} + T_{22})$. Choosing FPS (or equivalent CVFE) quadrature points defined via Eq. (31), it follows from Table 1 that if the local tensor field has a positive cross-term $T_{12} > 0$ for each cell the 9-point scheme reduces to a 7-point (triangle) scheme with diagonally upward positive-angle support as indicated in Fig. 5(a), by Table 1 $M_{15} = M_{19} = 0$ while the other off-diagonals are non-positive subject to Eq. (30). Conversely if $T_{12} < 0$ a diagonally downward negative-angle triangle support is obtained Fig. 5(b), in this case $M_{13} = M_{17} = 0$. We note that Eq. (30) is consistent with the triangle grid scheme M-matrix conditions presented in the next section. We shall refer to Eq. (31) as the double-family *optimal support condition*. We also note that this leads to the *upper M-matrix limit* for the cross coefficient $|T_{12}|$. However the condition of Eq. (31) gives a family of optimal support schemes *independently* of the M-matrix conditions. In general, the choice of quadrature defined by Eq. (31) for double-families leading to (*optimal support*) yields a family of schemes that will select a variable support depending upon the local tensor and orientation (sign of the cross-terms). These observations lead to a generalisation of the previous FPS formulation [22].

Optimal support relies on exact algebraic cancelation for reduced support, c.f. Table 2. If coefficients vary over subcells, while exact algebraic cancelation is unlikely, optimal support can still be achieved by anisotropy favoring triangulation [4] (where the sign of triangulation angle equals the sign of dominant principal direction angle), or by special case construction [23] provided the local principal directions are well defined. However, when local principal directions are varying the discretization support must adapt according to the change in principal direction. This is demonstrated in [4], where the triangulation is adapted according to principal anisotropy angle. If the principal axes orientation is positive relative to a quadrilateral cell, the cell is diagonally triangulated with positive angle, conversely a negative principal axes orientation leads to a negative-angle diagonal triangulation, which we term anisotropy favoring triangulation. Such a triangulation is presented below for FPS (triangle grid schemes) and compared directly with the quadrilateral schemes using anisotropic quadratures. For a general heterogeneous medium, no matter how the scheme is constructed e.g. [4,22] where problems

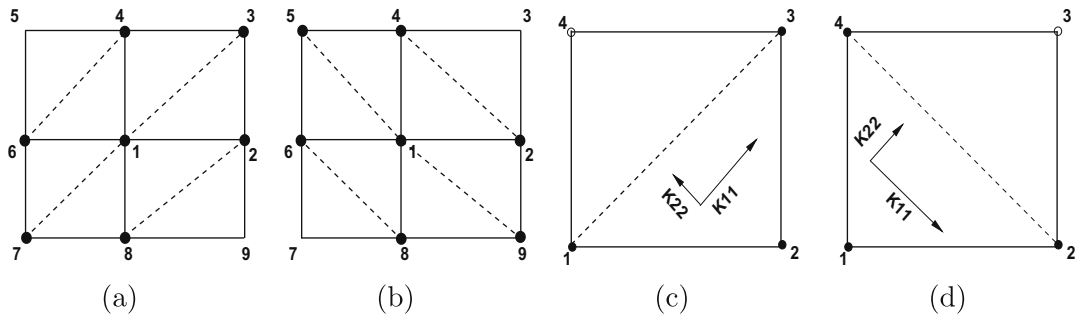

Fig. 5. (a) Positive T_{12} over all contributing dual-cells – right inclined 7 pt scheme (b) negative T_{12} over all contributing dual-cells – left inclined 7 pt scheme (c) positive T_{12} over a dual-cell (d) negative T_{12} over a dual-cell.

Table 2
Optimal support $\eta T_{11} + \xi T_{22} = |T_{12}|$ (FPS) *coefficients for constant tensor field.*

Integer coordinates	Coefficients	Full-tensor $T_{12} > 0$	Full-tensor $T_{12} < 0$
i,j	M11	$(2(T_{11} + T_{22}) - 2\|T_{12}\|)$	$(2(T_{11} + T_{22}) - 2\|T_{12}\|)$
$i+1,j$	M12	$-T_{11} + \|T_{12}\|$	$-T_{11} + \|T_{12}\|$
$i+1,j+1$	M13	$-\|T_{12}\|$	0
$i,j+1$	M14	$-T_{22} + \|T_{12}\|$	$-T_{22} + \|T_{12}\|$
$i-1,j+1$	M15	0	$-\|T_{12}\|$
$i-1,j$	M16	$-T_{11} + \|T_{12}\|$	$-T_{11} + \|T_{12}\|$
$i-1,j-1$	M17	$-\|T_{12}\|$	0
$i,j-1$	M18	$-T_{22} + \|T_{12}\|$	$-T_{22} + \|T_{12}\|$
$i+1,j-1$	M19	0	$-\|T_{12}\|$

involving variation in principal direction have been considered, or [23], determination of actual optimal support depends on an estimate of the tensor orientation over the cell (or dual-cell if cell-centred) where subcell fluxes are determined. In this work for a spatially varying tensor, the local tensor used for calculating the quadrature is determined by performing local upscaling with periodic boundary conditions over the primal cell [33] (or over the dual-cell if cell-centred). Note that if the optimal scheme is defined using Eq. (31) then the local optimal quadrature point is determined via the cell-wise upscaled general tensor, while the resulting scheme is applied to the original fine scale problem.

6.1. Anisotropic quadrature rules for optimal support

M-matrices are obtained if Eq. (29) is satisfied. If cross-terms vanish the quadrature Eq. (31) defaults to zero yielding the basic diagonal-tensor 5-point operator. Other M-matrix schemes that adapt quadrature according to the local tensor variation can also be defined provided other values of ξ, η can be found that lie in the range defined by Eq. (29). There are multiple advantages to the families of schemes. Certain quadrature points improve M-matrix bounds as discussed above, while others can improve accuracy. For example the single family with $\xi = \eta = 1/6$ leads to a sixth order accurate scheme in the case of Laplace's equation, while $\xi = \eta = 1/4$ defines the default finite-volume scheme and $\xi = \eta = 1/3$ defines the standard Galerkin method, [32]. Further important advantages are identified below for strongly anisotropic tensors.

We now consider highly anisotropic full-tensor fields where the M-matrix conditions are violated with $|T_{12}| > min(T_{11}, T_{22})$. The relationship between FPS and CVFE presented above shows that FPS is applicable for the whole CVFE quadrature range, while the pointwise continuous TPS schemes have limited quadrature range particularly for strong full-tensor anisotropy where they are not applicable, see the section on decoupling below.

We note that a family of optimal FPS schemes are defined via Eq. (31). As discussed above, for a spatially variable permeability field the grid cell tensor coefficients used for definition of the quadrature rule are local effective tensors and thus the analysis is expressed in terms of the resulting cell average tensors. We will denote optimal support (OS) quadrature points defining families of schemes via Eq. (31) by $\xi = \xi_{OS}, \eta = \eta_{OS}$. We may either choose a quadrature point with $\xi = \xi_Q$ such as a Gauss point and determine η_{OS} through Eq. (31), or choose $\eta = \eta_Q$ and determine ξ_{OS} through Eq. (31).

While the single-parameter family of FPS schemes will always remain within the quadrature range $0 \leqslant \eta < 1/2$ (by ellipticity) the double-family requires further consideration. Some specific examples that satisfy Eq. (31) are e.g. $(i)\xi = |T_{12}|/2T_{22}, \eta = |T_{12}|/2T_{11}$, (ii) $\xi = |T_{12}|/T_{22}, \eta = 0$, or (iii) $\xi = 0, \eta = |T_{12}|/T_{11}$. If we suppose that $T_{11} = max(T_{11}, T_{22})$, then $T_{22} = min(T_{11}, T_{22})$, and it follows that in case (i) $\xi = |T_{12}|/2T_{22} > 1/2$ (non valid quadrature) and $\eta = |T_{12}|/2T_{11} < 1/2$. In case (ii) $\xi = |T_{12}|/T_{22} > 1$ (non valid quadrature). Case (iii) is possible provided $|T_{12}|/T_{11} < 1/2$.

Thus the above considerations show that the optimal support quadrature parameter determined by Eq. (31) is that which multiplies the $max(T_{11}, T_{22})$, while the specified value multiplies the $min(T_{11}, T_{22})$, i.e. if $T_{11} = max(T_{11}, T_{22})$ then specify ξ_Q and determine η_{OS}. Similarly if $T_{22} = max(T_{11}, T_{22})$ then specify η_Q and determine ξ_{OS}. In the first case it follows from Eq. (31) that

$$\eta_{OS} = (|T_{12}| - \xi_Q T_{22})/T_{11} \tag{32}$$

which corresponds to quadratures ξ_Q, η_{OS} with ξ_Q specified and η_{OS} determined by

$$\eta_{OS} = (|T_{12}| - \xi_Q min(T_{11}, T_{22}))/max(T_{11}, T_{22}) \tag{33}$$

In this way the double-family is determined according to field anisotropy. The advantages here are that an optimal or approximately optimal scheme can be determined using a specified quadrature point such as a Gauss point that is away from the singular point for the first variable (ξ_Q in the above case), while the optimal quadrature point η_{OS} remains in the stable region. The effect of different quadrature values is presented in the results section.

6.2. Extreme anisotropic quadrature

Here we consider alternative anisotropic quadratures to that of the optimal support point, which are also motivated from the above observations. We define *extreme anisotropic quadrature* where for $T_{11} = max(T_{11}, T_{22})$ we set $\xi = 0, \eta \to 1/2$ and for $T_{22} = max(T_{11}, T_{22})$ set $\xi \to 1/2, \eta = 0$, the flux locations are illustrated in Fig. 6. Setting the quadrature multiplying the minimum diagonal to zero and maximising the second quadrature multiplying the maximum diagonal exploits the anisotropic flexibility of the method, while ensuring that the decoupled neighborhood where both $\xi \to 1/2, \eta \to 1/2$ is avoided. This offers an alternative quadrature that only requires $max(T_{11}, T_{22})$, where effective cell average properties are used if permeability has a spatial variation. Thus extreme anisotropic quadrature only has a weak dependence on the tensor coefficients, while the optimal support quadrature of Eq. (33) requires the actual tensor coefficients. An important advantage of extreme quadrature compared to any optimal support scheme is the independence from the angle of anisotropy which can vary in the general heterogeneous case. An optimal support scheme thus depends on a more sensitive upscaled general-tensor estimate in the general case, as the off-diagonal coefficients are used in determining the local direction of support, while extreme quadrature only needs to estimate which upscaled diagonal is the largest, i.e. if T_{22}/T_{11} is greater or less than one, the actual coefficients are not used. The results show that extreme quadrature yields solutions with resolution that is at least comparable with that of optimal support quadrature.

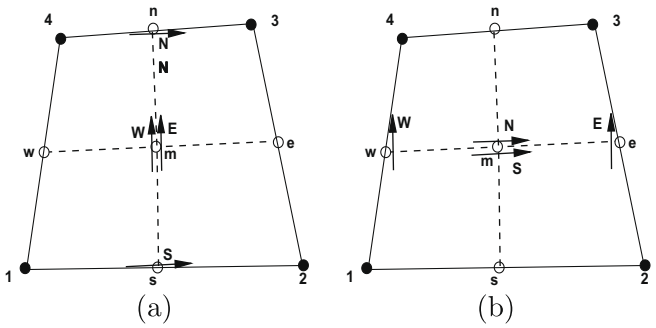

Fig. 6. Primary fluxes N, S, E, W in a cell (solid arrows): (a) extreme quadrature $\xi = 0.49, \eta = 0$, and (b) extreme quadrature $\xi = 0, \eta = 0.49$.

A further option is that extreme quadrature be employed locally in place of optimal support if (for a given ξ_Q) $\eta_{OS} > 1/2$, ensuring that the quadrature will remain in range.

6.3. Anisotropy and grid aspect ratio quadrature rules

Returning to the M-matrix bounds, another possibility suggested by Eq. (29) is to let

$$\eta T_{11} + \xi T_{22} = min(T_{11}, T_{22}) \tag{34}$$

This results in H or I reduced support schemes as in the case of the single family, and for strong full-tensor problems these schemes have the effect of spreading the solution [22]. For small or zero off-diagonal-tensor coefficients where $|T_{12}| \leqslant min(T_{11}, T_{22})$, schemes motivated by Eq. (34) become important. For the single family where $\xi = \eta$, it follows from Eq. (34) that $\eta = min(T_{11}, T_{22})/(T_{11} + T_{22})$ and η is effectively bounded by the minimum to maximum ratio of diagonal coefficients. Referring to Eq. (2) it follows that this ratio depends on both the permeability anisotropy ratio and local grid aspect ratio, which is seen immediately if e.g. $x_\eta = y_\xi = K_{12} = 0$, then from Eq. (2) $T_{11} = K_{11} y_\eta / x_\xi$ and $T_{22} = K_{22} x_\xi / y_\eta$. As the ratio $min(T_{11}, T_{22})/max(T_{11}, T_{22})$ decreases (e.g. if $K_{11} \sim K_{22}$ and large grid aspect ratio prevails with $(y_\eta/x_\xi)^2 \ll 1$) then $\eta \to 0$, and the scheme reduces to the standard five point operator. The flexibility offered by the double-family is again illustrated. Let us assume that $T_{22} = min(T_{11}, T_{22})$, then for the double-family one possibility is to set $\eta = 0$, then a family of H M-matrix schemes are defined by $0 \leqslant \xi < 1/2$.

7. Decoupled approximation

The quadrature point $\xi = \eta = 1/2$ is a decoupled point for the above CVFE, FPS and earlier TPS approximations, since the resulting discretization permits a *checker board* solution that is strongly oscillatory and decoupled, [22] varying with $\phi_{i,j} = +1$ together with diagonally connected neighbours where $\phi_{i\pm1,j\pm1} = +1$, while $\phi_{i\pm1,j} = -1$ and $\phi_{i,j\pm1} = -1$. This is verified by substituting $\xi = \eta = 1/2$ in Table 1 and testing the resulting operator on the checker board solution. For highly anisotropic full-tensors both the TPS single and TPS double-families are contained in the small end-interval c.f. Eq. (23), where $(\xi, \eta) \to (1/2, 1/2)$ for highly anisotropic full-tensors, which therefore leads to decoupling [22]. (The optimal quadrature point lies outside the TPS quadrature range when $|T_{12}| > 2T_{11}T_{22}/(T_{11} + T_{22})$ [22] which holds in the test cases below).

7.1. Flux filtering of decoupled modes

We note that the constant tensor-coefficient flux components of Eq. (20) also permit such a checker board solution mode with $\xi = \eta = 1/2$, then the fluxes take the form

$$\begin{aligned} F_S &= -\tfrac{1}{2}\left(T_{11}\left((\phi_2 - \phi_1)\tfrac{1}{2} + (\phi_3 - \phi_4)\tfrac{1}{2}\right) + \tfrac{1}{2}T_{12}((\phi_4 - \phi_1) + (\phi_3 - \phi_2))\right) \\ F_W &= -\tfrac{1}{2}\left(\tfrac{1}{2}T_{12}((\phi_2 - \phi_1) + (\phi_3 - \phi_4)) + T_{22}\left((\phi_4 - \phi_1)\tfrac{1}{2} + (\phi_3 - \phi_2)\tfrac{1}{2}\right)\right) \end{aligned} \tag{35}$$

and with locally numbered ϕ values corresponding to the checker board solution viz, $\phi_1 = 1, \phi_2 = -1, \phi_3 = 1, \phi_4 = -1$, it follows from Eq. (35) that

$$F_S = 0, F_W = 0.$$

The fluxes F_N, F_E also vanish under these conditions. This result indicates that the flux and therefore velocity field may not see the decoupled modes of a pressure field and they may in effect, be filtered from the flow solution. This has been observed in some two-phase flow results (results section case 3) obtained using the decoupled TPS pressure field solution, where the resulting saturation fields appear to be consistent with physical flow and appear free of spurious oscillations.

There are some important points to note here. First that the flow field results provide further evidence that the TPS pressure field has decoupled modes as discussed above. Second, while this may appear to suggest that decoupled fields may be useable for flow results, note that the TPS analysis leads to values of ξ, η in the neighbourhood of $\xi = \eta = 1/2$ for constant full-tensor fields at *high* anisotropy, but not necessarily at the exact point of 1/2. Consequently, we cannot be sure that the modes will completely cancel from the velocity field, particularly for variable coefficients and lower anisotropy ratios. Consequently such flow results cannot be regarded as reliable. Moreover experiments indicate that TPS based flow calculations can still lead to instabilities. Also note that the above observations are for strictly incompressible flow. Decoupling can be expected to have a further detrimental effect on velocity if flow is compressible, and of course for multi-phase flow a decoupled pressure field will be useless, particularly if phase changes are involved.

However, as discussed above, the FPS double-family approximation can be applied to all elliptic tensors and permit anisotropic quadratures that avoid the TPS decoupled zone while ensuring improved solution resolution.

7.2. Corollary: a monotone discretization matrix avoids decoupling

An obvious feature of a decoupled solution are the modes of oscillation between positive and negative values. Thus we may conclude that while a scheme with a monotone discretization matrix may not be able to guarantee that resulting numerical solutions are free of spurious oscillations, the monotone property is sufficient to prevent decoupling, since a monotone matrix ensures that any problem with non-negative boundary data yields a positive solution. This observation motivates the idea of constructing a monotone matrix scheme for high full-tensor anisotropy ratios. This property can be built into the approximation via a non-linear construction where scheme coefficients are functions of the solution as presented in [27,26]. The schemes presented here are linear with respect to the solution vector and while they are not monotone for the test cases considered, they are quasi-positive as defined below and prove to be beneficial.

8. M-matrix conditions for triangle grid schemes

A cell-wise M-matrix analysis is performed for the triangle grid scheme. Discrete cell-vertex fluxes on a triangle with interior discontinuous coefficients can always be expressed as a linear combination of edge differences as noted earlier, with $AF = -\Delta\Phi_v$ [28]. As a result, discrete flux components with respect to vertex 1 Fig. 4(a) are written as

$$F_i = -(T_{i1}(\phi_2 - \phi_1) + T_{i2}(\phi_3 - \phi_1)) \tag{36}$$

for $i = 1, 2$ where T_{ij} are local control-volume tensor coefficients derived from flux continuity conditions. The T_{ij} coefficients are functions of local subcell permeability, geometry and quadrature location. The net flux contribution for vertex 1 from the two triangle subcell faces S and N Fig. 4(a), is then

$$F = -((T_{11} + T_{21})(\phi_2 - \phi_1) + (T_{12} + T_{22})(\phi_3 - \phi_1)) \tag{37}$$

Gathering coefficients of the diagonal pressure ϕ_1 and off-diagonal pressures ϕ_2, ϕ_3 respectively, it follows that cell-wise M-matrix conditions with positive diagonal M_{11} and negative off-diagonals $M_{1j}, j \neq 1$ will be obtained if

$$|T_{21}| < T_{11}, \quad |T_{12}| < T_{22} \tag{38}$$

Cell-wise diagonal dominance also follows with $M_{11} = |M_{12}| + |M_{13}|$ with strict inequality for at least one row due to the essential Dirichlet condition. Symmetry does not hold in physical space for an arbitrary triangle and permeability tensor. However, if special cases occur where symmetry of the general tensor is obtained it follows directly from Eq. (38) that

$$|T_{12}| < min(T_{11}, T_{22}) \tag{39}$$

This key result of [29], is consistent with the quadrilateral optimal support M-matrix analysis c.f. Eq. (30) above.

9. Quasi-positive QM-matrices

In this section we introduce the notion of quasi-positivity in reference to matrices that suffer a *small violation* of the M-matrix property.

Definition: We define a Quasi-M-matrix or QM-matrix as a matrix with only two positive off-diagonal coefficients per row that violate the M-matrix conditions. [22].

This definition is motivated by the spatially constant tensor coefficient case c.f. Table 1.0. Inspection of Table 1.0 reveals that the matrix coefficients are symmetric and therefore the minimum number of positive off-diagonal coefficients violating the M-matrix conditions is two.

While the general tensor will vary according to the local permeability and grid geometry and lead naturally to local variation in the matrix coefficients across the field, the constant coefficient case still provides much insight into the behaviour these schemes. M-matrix limits have been presented above, and the first example presented below (see results section), illustrating the occurrence of problematic spurious oscillations when using TPS, involves a spatially constant full-tensor field where the M-matrix limits are violated. Therefore in this case analysis of the spatially constant tensor coefficient case is

exact and applies directly. We also emphasize that the discussion of beneficial quadrature points below is in reference to FPS as TPS is not practical for such cases.

Here we consider elliptic tensors where the fundamental M-matrix (and monotone matrix) conditions are violated i.e. when

$$|T_{12}| > min(T_{11}, T_{22}) \tag{40}$$

Note by ellipticity we always have $|T_{12}| < max(T_{11}, T_{22})$. In the case of Eq. (40), for a spatially constant tensor Table 1.0 reveals that there are certain intervals for which there is one unique offending *positive* off-diagonal coefficient, by matrix symmetry c.f. Table 1.0, and consequently we need only consider the signs of $M_{12}, M_{13}, M_{14}, M_{15}$ to determine the QM-matrix ranges. The range of positive coefficient intervals is presented in [22] for the single family and illustrated here in Fig. 7(a) for the tensor of Eq. (42) used in test case 1 below, note that $T_{11} = max(T_{11}, T_{22})$ in this case, where the grid has unit aspect ratio. The double-family permits an entire quadrature field of QM-matrices, illustrated in Fig. 7(b) for the same case. Note that there is always at least one unique positive off-diagonal coefficient visible in Figs. 7(a) and (b) and 8(a) and (b) which verifies violation of the M-matrix conditions. Comparing Fig. 7(a) for the single family and Fig. 7(b) for the range of double-families shows that the double-families yield a wider class of QM-matrices than the single parameter family. For example set $\eta = 0$ in Table 1, then $M_{15} > 0$ for all $0 \leqslant \xi < 1/2$, is the only unique positive off-diagonal, while the others remain negative, Fig. 8(a), which does not occur for a single family. The single family is also compared directly with the double-family by including the

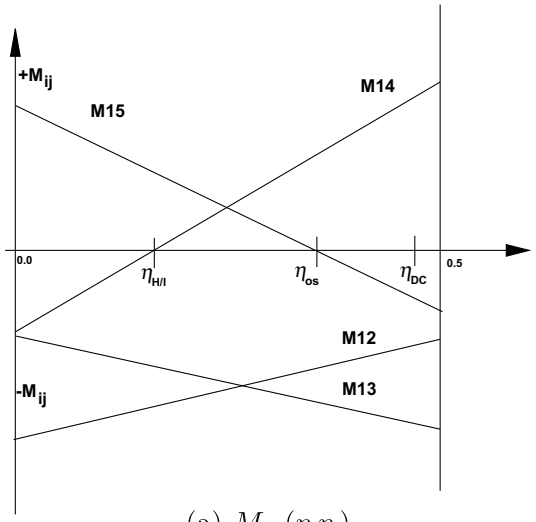

(a) $M_{1j}(\eta,\eta)$

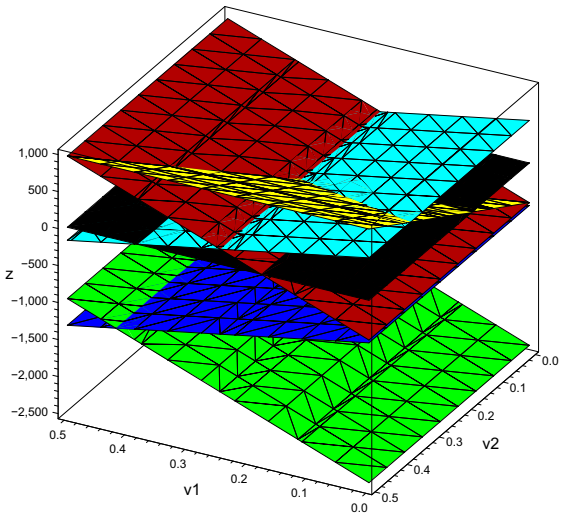

(b) $M_{1j}(\xi,\eta)$planes:Zeroplaneisblack

Fig. 7. Unique coefficients M12, M13, M14, M15 (quadrature ranges): (a) single family $\xi = \eta$, and (b) double-family planes.

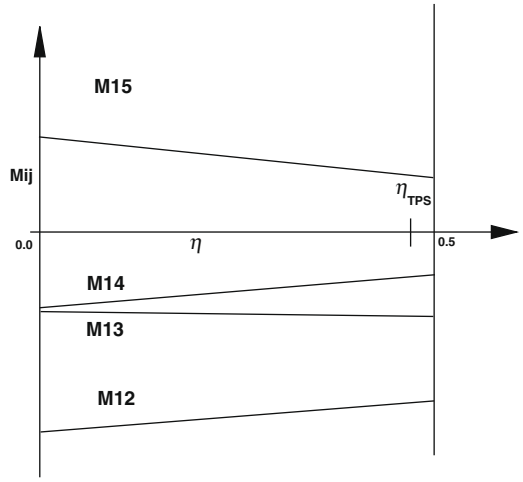

(a) $M_{1j}(\xi, 0)$

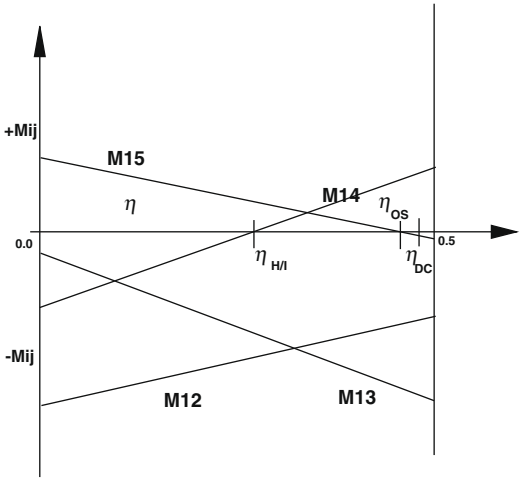

(b) $M_{1j}(0,\eta)$

Fig. 8. Unique coefficients M12, M13, M14, M15 (quadrature ranges): (a) double-family $0 \leqslant \xi < 1/2; \eta = 0$, and (b) double-family $\xi = 0; 0 \leqslant \eta < 1/2$.

single family matrix coefficient $M_{14}(\eta, \eta)$ in the double-family diagram of planes of unique matrix coefficients Fig. 7(b). The $M_{14}(\eta, \eta)$ coefficient is an extrapolated single family plane cutting through the double-family planes in Fig. 7(b), indicating regions where double-families yield improved QM-matrices compared to a single family e.g. for $0 \leqslant M_{14}(\xi, \eta) \leqslant M_{14}(\eta, \eta)$. From Eq. (31), the *optimal* support quadrature obtained via the double-family formulation yields a family of optimal support schemes, and thus larger quadrature range compared to the single family which has a single optimal support quadrature point.

Optimal support quadrature points are also optimal with respect to a QM-matrix, since i) they correspond to a point where there is only one violating coefficient out of the four possible coefficients $M_{12}, M_{13}, M_{14}, M_{15}$, and ii) the violating coefficient has a minimum positive value. The term minimum is used here with respect to the constraint that the coefficient is M-matrix violating. For example, for the single family the unique coefficient $M_{14} \geqslant 0$ is minimised at η_{OS}, Fig. 7(a). For the double family a particular example is presented in Fig. 8(b) for the range $(\xi = 0, 0 \leqslant \eta < 1/2)$ where η_{OS} is indicated. In both the single and double-family cases M_{14} is positive at η_{OS} (c.f. Table 2) and is increasing to the right of η_{OS}, while to the left of η_{OS} two coefficients (M_{14} and M_{15}) are now positive, leading to a total of four actual positive matrix coefficients that violate the M-matrix conditions. While $0 \leqslant \eta \leqslant \eta_{HI}$ (where η_{HI} originates from Eq. (34)) defines a further range of QM-matrices where only $M_{15} > 0$, these schemes do not correspond with the full-tensor anisotropy direction and are found to spread the solution. This is also discussed in [22], where a study of the effects of the full range of quadrature for the single FPS family is presented.

While the optimal points yield well resolved fields, consistently good resolution is also obtained for distinctly different ξ and η chosen according to extreme anisotropic quadrature discussed earlier. For example if $T_{11} > T_{22}$ then $\eta \to 1/2$ while $\xi \to 0$, the matrix coefficients in this case are illustrated in Fig. 8(b), where it is seen that the scheme still has a QM-matrix. This strategy is unique to the double-family formulation in 2-D and has proven to be highly effective. While the leading quadrature parameter is chosen according to strength of the dominant diagonal-tensor coefficient, crucially the values of quadrature are otherwise independent of the tensor coefficients when chosen in this way. For a spatially varying tensor field extreme quadrature provides an important advantage and simplification as discussed above due to being independent of principal direction. All optimal support schemes including [4,22,23] and those presented above depend on an estimate of the principal direction to define the scheme support.

9.1. QM-matrices on triangles

We note that (i) All cell-vertex triangle grid schemes share the same form of cell-wise M-matrix limit c.f. Eq. (39), as that of the optimal schemes presented above. (ii) Results computed using triangular grids appear to be quite robust with respect to different triangulations. The latter observations suggest that cell-vertex triangle grid schemes may possess QM-matrices for general triangulations. Tests of the schemes on triangulations (where the schemes are not generally symmetric) for positive off-diagonal coefficients has thus far indicated that up to three coefficients per row can be positive. Since the above QM-matrix definition has arisen from symmetric constant coefficient schemes where a strict minimum number of two positive off-diagonals is identified, this may be reconciled by revising the QM-matrix definition to allow for the general non-symmetric case, e.g. permit up to three positive off-diagonal coefficients in the non-symmetric case.

However, triangulation of a quadrilateral grid that favors anisotropy conforms with the original definition and leads to optimal QM-matrices for the FPS formulation where the same seven-point optimal support is obtained, with only two positive off-diagonal coefficients.

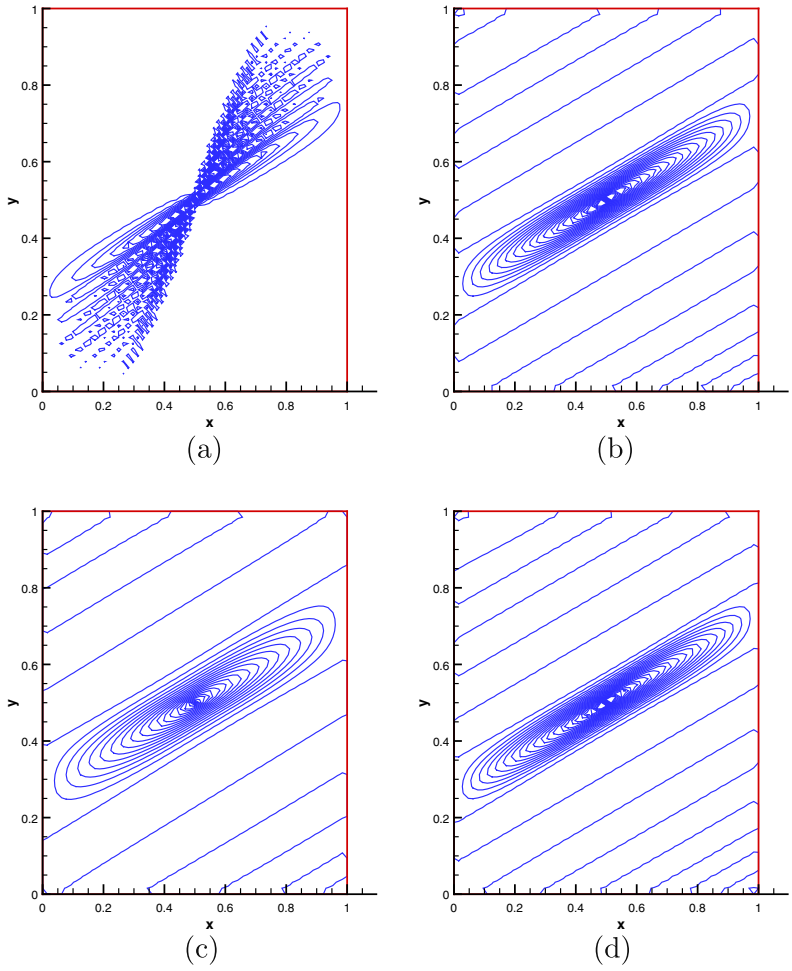

Fig. 9. Cartesian grid, homogeneous: (a) TPS $p = 1$, $q = 0.0001$, (b) FPS optimal $\xi_{\text{Gauss}}, \eta_{\text{OS}}$, (c) FPS extreme counter-anisotropy $\xi = 0.49, \eta = 0$, and (d) FPS extreme favoring-anisotropy $\xi = 0, \eta = 0.49$.

10. Numerical results

Comparisons are presented between the new full-pressure support FPS double-family formulation and the earlier pointwise continuous TPS formulation for domains with full-tensors with strong cross-terms that violate the M-matrix conditions.

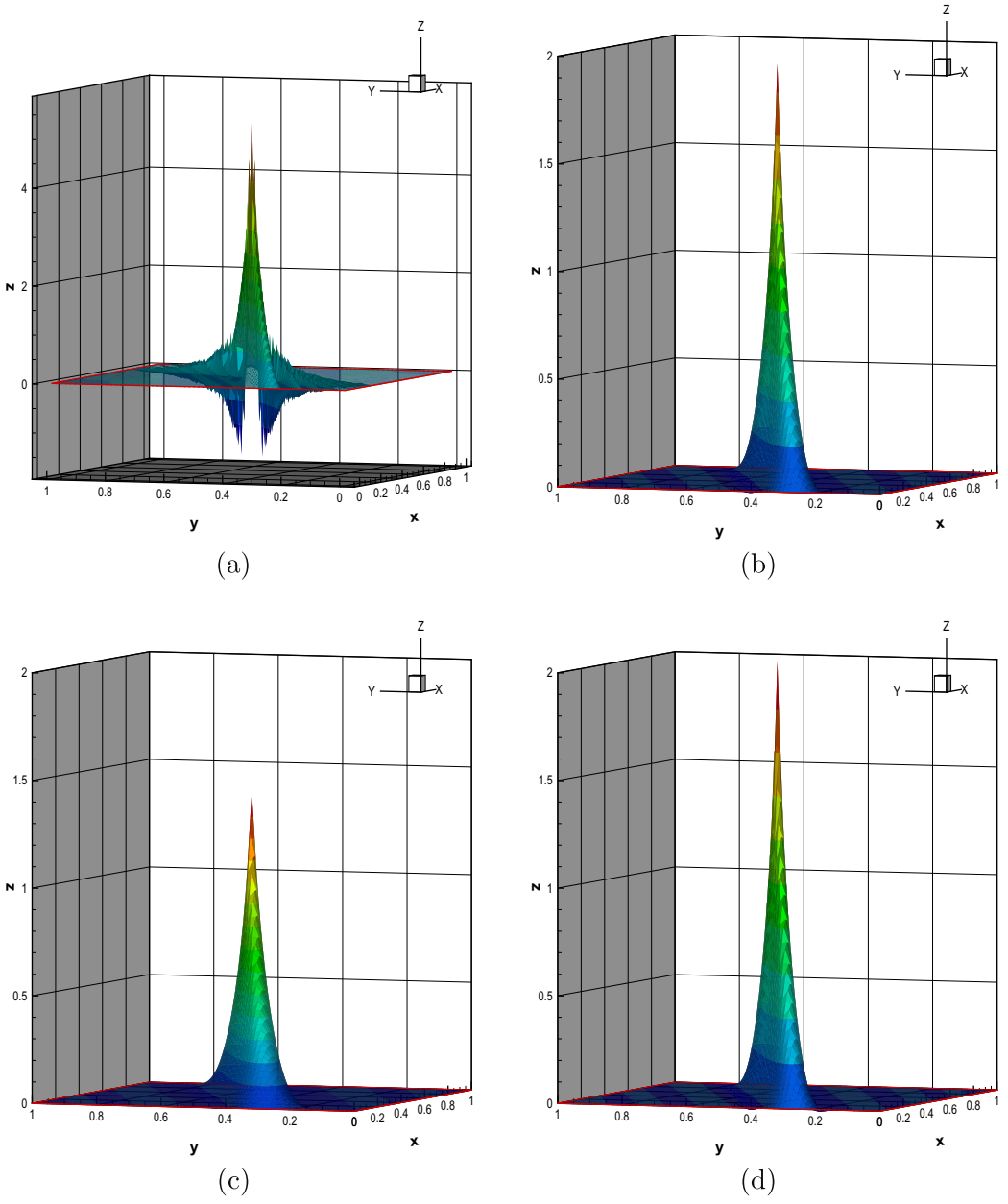

Fig. 10. Cartesian grid, homogeneous: (a) TPS $p = 1$, $q = 0.0001$, (b) FPS optimal $\xi_{\text{Gauss}}, \eta_{\text{OS}}$, (c) FPS extreme counter-anisotropy $\xi = 0.49, \eta = 0$, and (d) FPS extreme favoring-anisotropy $\xi = 0, \eta = 0.49$.

Table 3
Discrete maximum principle test.

Scheme	No. of violation	Max	Min
TPS $p = q = 1$	162	5.5240	−1.5937
FPS OS	20	1.9350	−0.0466
FPS ($\xi = 0$, $\eta = 0.49$)	20	2.0232	−0.0486
FPS ($\xi = 0.49$, $\eta = 0$)	4	1.3518	−0.0311

As with the TPS family, the new FPS families of schemes are exact for piecewise linear test cases with jumps in full-tensor permeability. However unlike TPS, the FPS flux formulation is also exact for piecewise bilinear test cases with jumps in full-tensor permeability, consistent with the FPS subcell bilinear basis functions, c.f. Case 0 below and Appendix A. Convergence behaviour has been found to match that of the TPS schemes for lower anisotropy ranges. The test cases presented demonstrate the advantages of the FPS methods in terms of quasi-positivity.

10.1. Case 0: piecewise bilinear field

The following test involves Poisson's equation (Appendix A). A piecewise bilinear field is defined over $\Omega = [0,1]X[0,1]$ and involves a permeability field with a discontinuity at $x = \frac{1}{2}$, with the left and right-hand tensors are defined by $K_L(x,y)$ for $0 \leqslant x \leqslant 1/2$ and $K_R(x,y)$ for $1/2 < x \leqslant 1$ respectively, where

$$K_L(x,y) = \begin{pmatrix} 1 & 0.5 \\ 0.5 & 1 \end{pmatrix}, \quad K_R(x,y) = \begin{pmatrix} 10 & 2 \\ 2 & 100 \end{pmatrix} \tag{41}$$

The exact pressure field is defined by

$$\phi = \begin{cases} 10 + 20xy, & x \leqslant \frac{1}{2} \\ 10.75 - 1.5x + 9y + 2xy, & x > \frac{1}{2} \end{cases}$$

Dirichlet boundary conditions are imposed on all boundaries with data defined by the exact solution. The FPS schemes yield the exact solution within six decimal places for all quadrature points tested. The TPS schemes have a convergence rate of approximately unity for this problem.

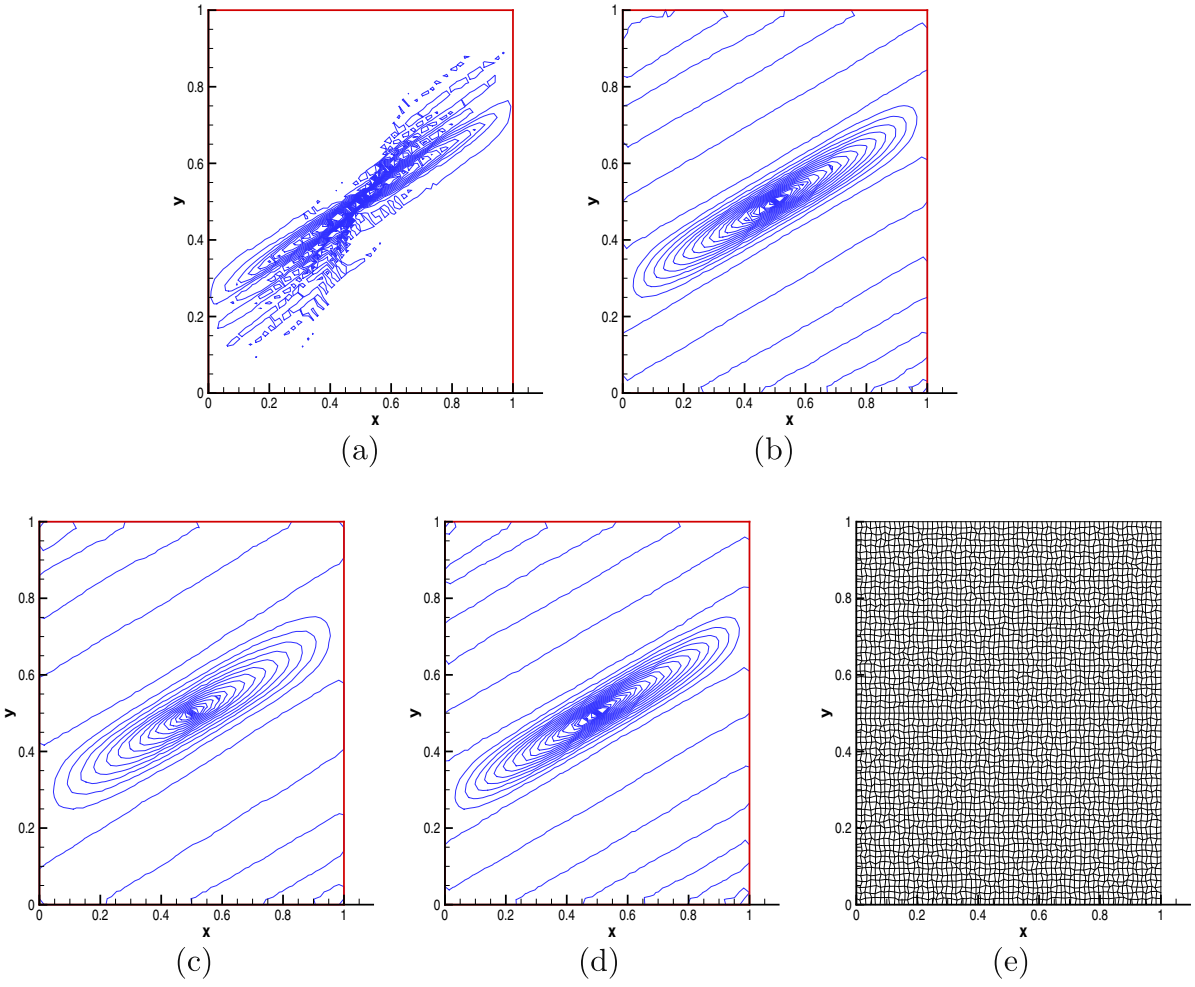

Fig. 11. Perturbed quadrilateral grid, homogeneous tensor: (a) TPS $p = 1$, $q = 0.0001$, (b) FPS optimal $\xi_{\text{Gauss}}, \eta_{\text{OS}}$, (c) FPS extreme counter-anisotropy $\xi = 0.49, \eta = 0$, (d) FPS extreme favoring-anisotropy $\xi = 0, \eta = 0.49$, and (e) quadrilateral perturbed mesh.

10.2. Case 1: planar full-tensor field

The first case with results presented, involves a uniform anisotropic medium with a point source in the middle of a unit square domain. Dirichlet boundary conditions are applied with pressure set to zero on all boundaries. The full-tensor is given by

$$\mathbf{K} = \begin{pmatrix} 2464.360020 & 1148.683643 \\ 1148.683643 & 536.6399794 \end{pmatrix} \tag{42}$$

with high anisotropy ratio 3000:1 and grid *non-aligned* with the principal axes, which are oriented at an angle of 25 degrees to the computational grid, leading to a full-tensor. The full-tensor field violates the M-matrix condition. First a quadrilateral scheme is used in each case, with 65×65 grid resolution.

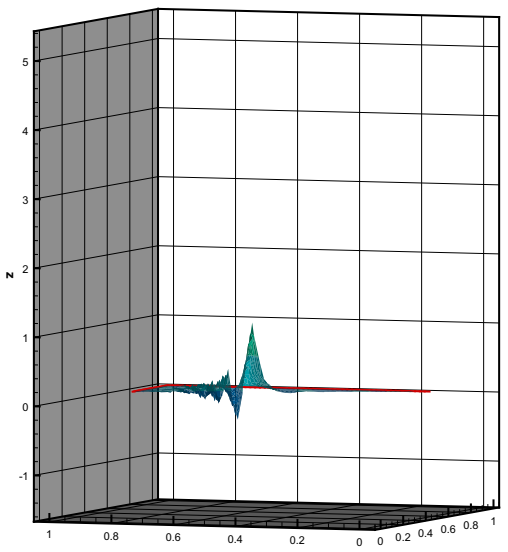

Next we present the new FPS double-family results for an optimal scheme (b), where an example optimal point, using the Gauss point $\tilde{\xi} = 1/\sqrt{3}$ is selected and where η_{OS} is defined via Eq. (31) leading to quadratures ξ_{Gauss}, η_{OS} yielding a well resolved solution, Figs. 9(b) and 10(b). Next in (c) counter extreme anisotropic quadrature is employed with $\xi = 0.49, \eta = 0$, i.e. against anisotropy, resulting in Figs. 9(c) and 10(c). Finally (d) extreme anisotropic quadrature favoring the anisotropy with $\xi = 0, \eta = 0.49$, yielding results shown in Figs. 9(d) and 10(d), respectively. Results (b), (c) and (d) each correspond to QM-matrices and no spurious oscillations are seen in this case. As expected (c) yields the smoother solution. Result (b) uses an optimal point with reduced support favoring anisotropy. The solution is well resolved by (b) and (d). Note that anisotropy motivated extreme quadrature (d) yields sharper resolution than the optimal point scheme (b).

We present a comparative analysis of discrete maximum principle violation in Table 3 below. The criterion for violation is if Eq. (25) is violated, i.e. if $\phi_i > \phi_{imax}$ or $\phi_i < \phi_{imin}$ where ϕ_{imax}, ϕ_{imin} are the respective maximum and minimum values of pressure at the neighbouring nodes belonging to the support of node *i*. The global maximum and minimum values of pressure are also listed. The test detects violations in the fourth decimal place. A scheme that eliminates DMP violations is presented in [24].

10.2.1. Case 1: planar field, using perturbed quadrilateral grid

The same case is tested using a perturbed quadrilateral grid, the results are shown in Figs. 11(contours) and 12(isosurfaces), the grid is shown in Fig. 11(e). Again the pointwise continuous TPS scheme suffers from strong oscillations, while both the optimal point (Figs. 11(b) and 12(b)) and favorable extreme anisotropic quadrature schemes (Figs. 11(d) and 12(d)) yield similar sharp results demonstrating that their properties also apply to grids with distorted cells comprised of more general geometry.

10.2.2. Case 1: planar field, using triangular grids

Next we consider the triangle cell-vertex scheme. Results are compared for two 65×65 grids, with triangulations illustrated by Fig. 13(a) and (b). For the grid with triangulation in the counter direction to anisotropy the solution is smoother

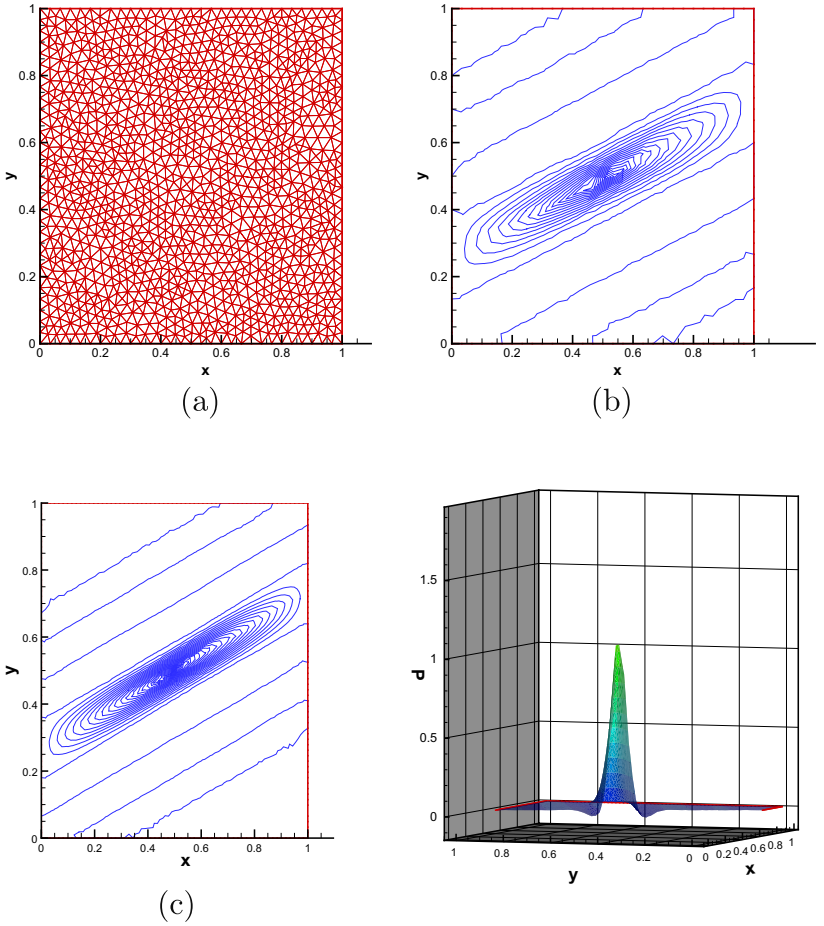

Fig. 14(a) and (b), while for the grid with triangulation favoring anisotropy the solution is well resolved Fig. 14(c) and (d), consistent with the optimal support favoring anisotropy. We note that there is an analogous improvement in solution resolution when using anisotropy favoring quadrature and anisotropy favoring triangulation.

A range of *Delaunay Triangulations* have also been used for the same test case. A 1283 node grid and contours are shown in Fig. 15(a) and (b), the solution is well resolved on the finer 5230 node grid Fig. 15(c) and (d). The results indicate that the cell-vertex FPS method is quite robust with respect to triangulation.

10.3. Case 2: strong discontinuous full-tensor (Zigzag) field

In this case the boundary conditions for the unit domain involve a constrained pressure source-sink configuration placed at diagonally opposite corners of the domain. The bottom left hand corner pressure is set to 0.0 and the top right-hand corner pressure is set to 200, together with pressure set to 100 on all boundary walls. The permeability tensor changes direction in anisotropy at one third and two thirds the way across the domain. The discontinuous full-tensor permeability field is defined in sections with sign of cross-terms varying, the tensor of Eq. (42) is assigned to the first and third sections and with

$$\mathbf{K} = \begin{pmatrix} 2464.360020 & -1148.683643 \\ -1148.683643 & 536.6399794 \end{pmatrix} \tag{43}$$

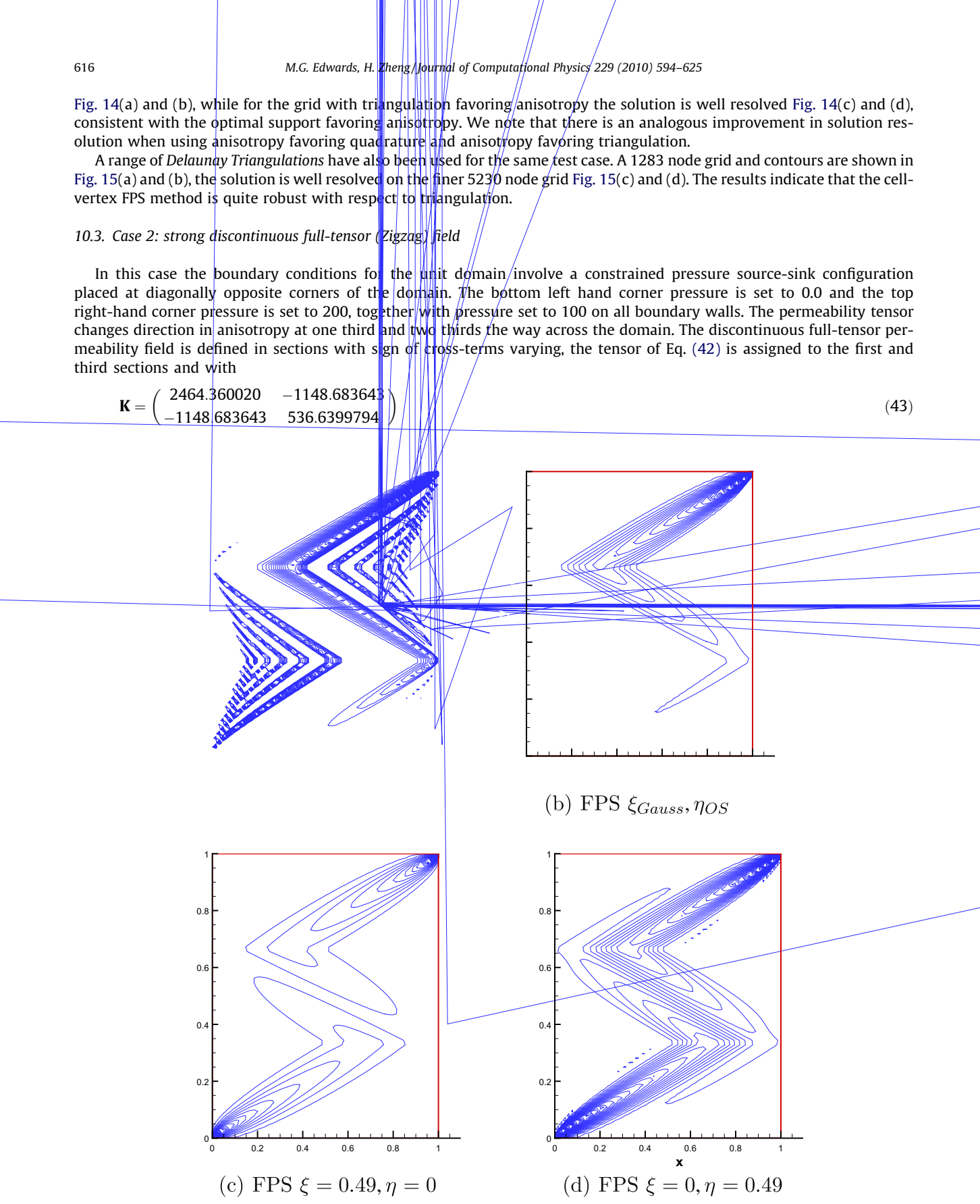

Fig. 16. (a) TPS-quadrilateral, (b) FPS-quadrilateral: $\xi_{\text{Gauss}}, \eta_{\text{OS}}$, (c) FPS extreme counter-anisotropy: $\xi = 0.49, \eta = 0$, and (d) FPS extreme favoring-anisotropy: $\xi = 0, \eta = 0.49$.

in the second section. At each section the principal axes are oriented at an angle of 25 degrees, (i.e. plus, minus, plus 25 degrees) to the computational grid. The tensor again has a principal anisotropy ratio of 3000:1, violating the M-matrix condition in each section. Quadrilateral scheme results are presented in Figs. 16 and 17. The grid has 65×65 resolution with control-volume boundary alignment on the interfaces between jumps in the permeability tensor.

Results are presented for the TPS scheme in Fig. 16(a) and 17(a), the condition of Eq. (31) is not satisfied by the TPS scheme due to the smaller quadrature range. There are very strong oscillations in the TPS solution (which remains positive) showing clear violation of the maximum principle as expected from the M-matrix and decoupling analysis.

We now compare with the FPS double-family schemes. A locally upscaled tensor is used to define the quadrature over the dual-cell (with resulting optimal scheme applied to the original permeability field), which yields a mean tensor for regions where permeability varies, in this case along the sub-domain boundaries where permeability is discontinuous. The exact tensor is otherwise obtained where the field is spatially constant over the cell.

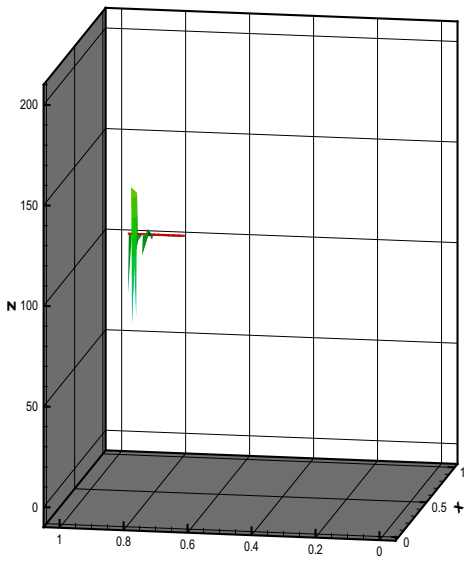

An optimal scheme quadrature point $(\xi_{\text{Gauss}}, \eta_{\text{OS}})$ is again defined via Eq. (31). In this case away from the discontinuities the support of the scheme reduces such that the scheme has *optimal support* that favors anisotropy. Thus away from the discontinuities the FPS schemes essentially lead to angled approximations according to local orientation of the full-tensor field, Fig. 5. The solution is well resolved and essentially free of spurious oscillations, Figs. 16(b) and 17(b).

Next in (c) FPS employs extreme counter-anisotropic quadrature with $\xi = 0.49, \eta = 0$ (i.e. against anisotropy), resulting in Fig. 16(c) and 17(c), leading to a diffused solution. Finally (d) FPS with extreme anisotropic quadrature favoring the anisotropy with $\xi = 0, \eta = 0.49$, yields the results in Figs. 16(d) and 17(d) respectively. While a small number of oscillations are visible, the extreme quadrature scheme result (d) shows that the method consistently yields slightly sharper resolution than the optimal point scheme. As before the FPS methods yield results that are almost free of spurious oscillations with quasi-positive solutions for both planar and discontinuous full-tensor permeability fields. Both optimal point and extreme quadratures are found to be beneficial.

10.3.1. Case 2: Strong full-tensor (Zigzag) field, using a triangular grid

Next we test the triangular grid FPS scheme using a triangulation favoring the anisotropy. The grid has the same resolution as the previous case. An illustrative coarse grid is shown in Fig. 18(a). A boundary aligned grid (BAG) is employed where control-volume faces are aligned with interior boundaries across which permeability jumps and is discontinuous, the grid is illustrated in Fig. 18(b). This grid naturally yields an optimal support scheme due to the anisotropy favoring triangulation discussed above. The triangular grid results Fig. 18(c) and (d) are in very good agreement with the optimal point quadrilateral grid results Fig. 16(b) and 17(b).

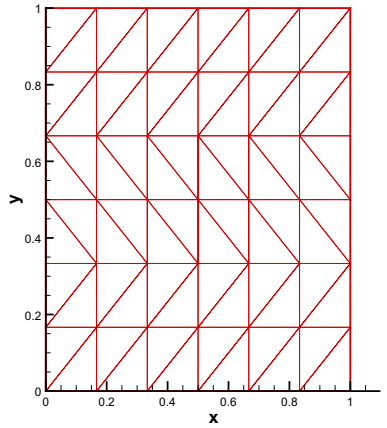

(a) Triangle Grid

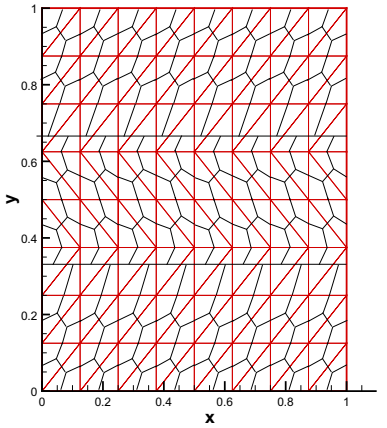

(b) Control-volume Grid

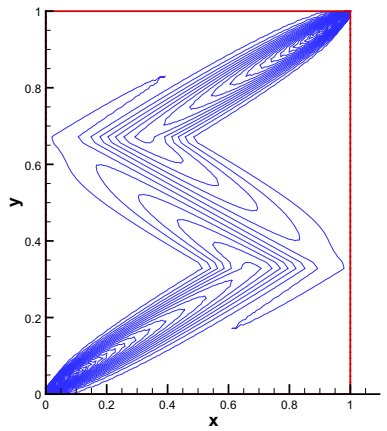

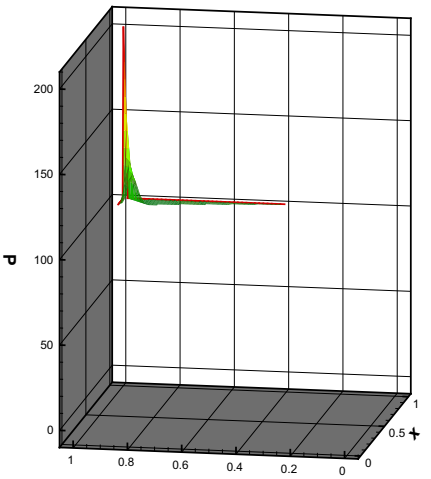

(c) FPS Triangles

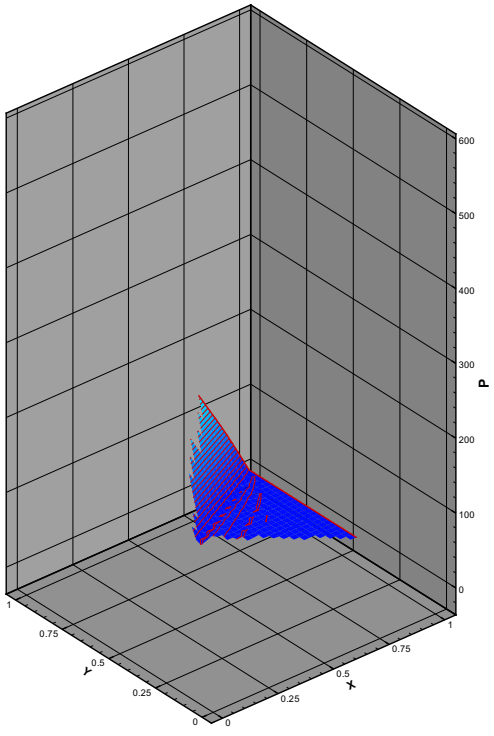
600
500
400
300
200
100
0
P
1
0.75
0.5
0.25
0
Y
0
0.25
0.5
0.75
1
X

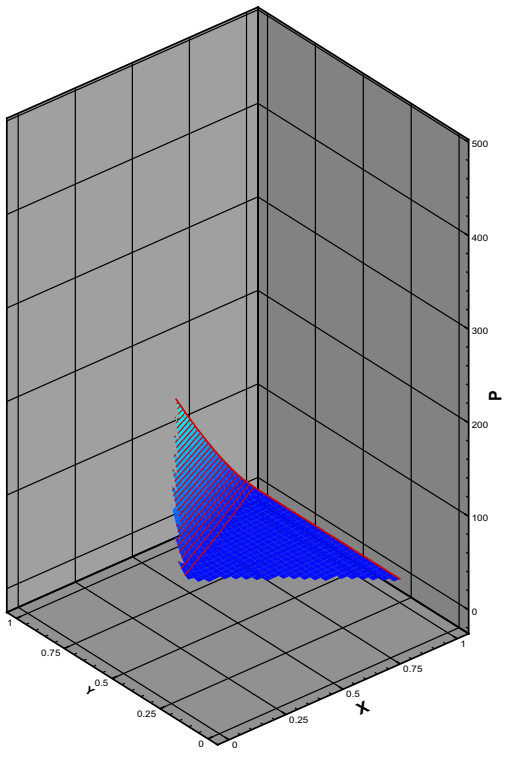
500
400
300
P
200
100
0
1
0.75
0.5
0.25
0
Y
0
0.25
0.5
0.75
1
X

10.4. Case 3: two-phase flow

This case shows the discretization effects of FPS and TPS in the case of two-phase flow in an anisotropic channel, with permeability tensor given by Eq. (42). Planar injection of water into a square domain $\Omega([0,1]\times[0,1])$ initially filled with oil is considered.

Further details for the two-phase flow system are presented in [3], and we refer to [34] for general multi-phase flow equation details. Here we simply state the additional continuity phase equation for water saturation s, where

$$\int_\Omega \left(\frac{\partial s}{\partial t} + \nabla\cdot(\mathrm{f}(s)\mathbf{u_T})\right)\mathrm{d}V = 0 \tag{44}$$

away from sources/sinks. Here $\mathrm{f}(s)$ is the fractional flow, the total velocity $\mathbf{u_T} = -\Lambda\mathbf{K}\nabla\phi$, where total mobility Λ is a function of s. The total velocity satisfies the incompressibility condition

$$\int_\Omega \nabla\cdot\mathbf{u_T}\mathrm{d}V = 0 \tag{45}$$

The system Eqs. (44), (45) is solved using the classical implicit pressure explicit saturation (IMPES) formulation with forward Euler time stepping. Single-point upstream weighting (first order upwind) is used for the saturation equation convective flux approximation. Truly multi-dimensional and higher order methods are presented in [31]. The pressure equation Eq. (45) is solved using the methods presented above.

Two types of left hand boundary condition are considered; (a) fixed flow rate, (b) fixed pressure, with left hand boundary water saturation $s(0,y,t) = 1$ for both cases. Initially $s(x,y,0) = 0$ through out the domain. In both cases, zero normal flow boundary conditions are applied on the top and bottom walls and pressure is specified on the right-hand exit boundary. These cases do not involve point singularities as in the previous examples, but involve both Neumann and Dirichlet boundary conditions. A uniform 41×41 cartesian grid is used for these cases. The medium is uniformly anisotropic with tensor defined by Eq. (42) above.

10.4.1. Case 3(A)

For the rate constrained problem, the physical solution is radically different to the pressure constraint case 3(B), c.f. comparing the FPS pressure solutions and saturation fronts Figs. 20(a) and (b) and 23(a) and (b), the difference is attributed to the strongly oriented anisotropy of the full-tensorial field.

In case 3A, the constrained rate problem leads to a single finger that dominates the Buckley Leverett saturation field and moves to break through at the outflow boundary. While the TPS pressure field exhibits some signs of decoupling Fig. 19(a), this is quite mild compared to case 3(B). The appearance of non-physical local extrema on the inflow boundary is also evident in Fig. 19(a). In contrast the FPS favorable extreme quadrature scheme yields a stable pressure field Fig. 20(a). Saturation fields are shown at $0.35\,pv$ (pv or pore-volumes injected). The TPS saturation front Fig. 19(b) indicates some physical features that are qualitatively similar to FPS Fig. 20(b), but also exhibits a saw-tooth profile.

10.4.2. Case 3(B)

Pressure is specified on the left and right-hand boundaries with $\phi_L = 1, \phi_R = 0.1$. No flow zero normal flux conditions are applied on the top and bottom boundaries.

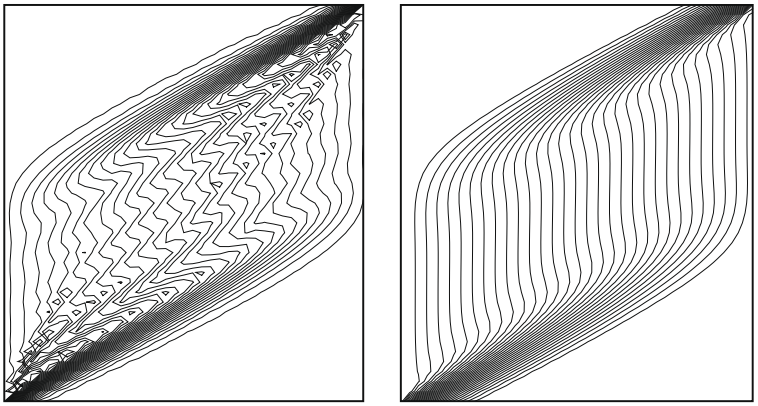

(a) TPS pressure (b) FPS pressure

Fig. 21. Channel B: specified pressure: (a) TPS pressure contours, and (b) FPS pressure contours.

The pressure field contours and isosurfaces obtained using TPS are shown in Figs. 21(a) and 22(a), respectively, where spurious oscillations dominate the solution, as in the previous examples, even for this seemingly innocent test case. The pressure field contours and isosurfaces computed using the FPS favorable extreme anisotropy scheme are stable and well resolved and shown in Figs. 21(b) and 23(a), respectively. The optimal scheme pressure field (not shown) is practically the same as the favorable extreme quadrature result.

In this case the flow saturation is dominated by formation of a piston displacement front over the lower portion of the domain which moves along the principal direction towards the outflow boundary. The saturation isosurfaces are shown at time $0.35pv$, Fig. 22(b) corresponds to the saturation computed using the TPS scheme for pressure, and Fig. 23(b) corresponds to the saturation computed using FPS with extreme quadrature favoring the anisotropy for pressure. The two satu-

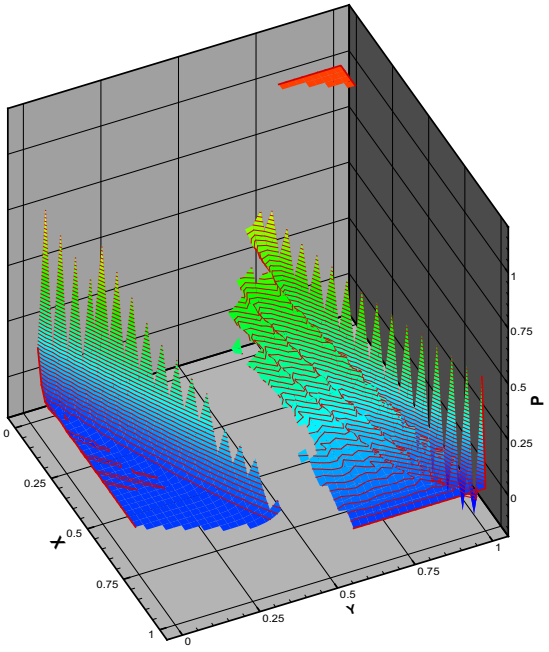

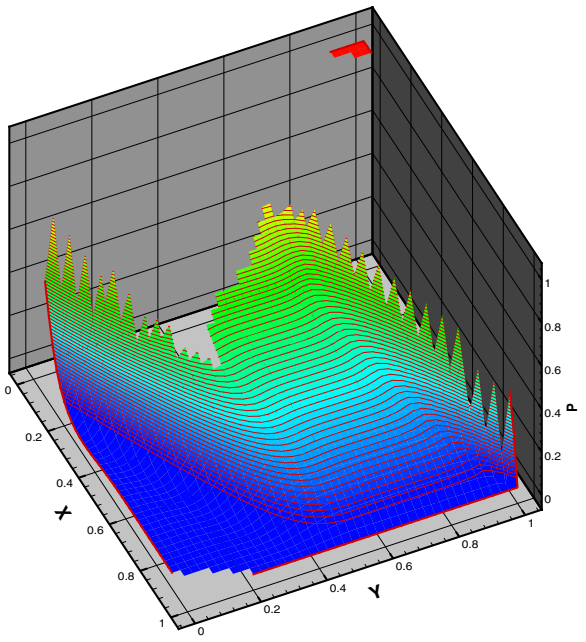

ration fields are quite similar in this case. No spurious oscillations are observed in either of the saturation plots, which is quite remarkable for TPS. We note that this result is consistent with the observation from Eq. (35), where it is shown that the fluxes evaluated at $\xi = \eta = 1/2$ effectively cancel out decoupled solution modes. Consequently it is possible for the TPS flux to filter the oscillations by cancelation of the spurious modes, TPS has an equivalent quadrature of 0.4994 in this case, which is very close to the decoupled value of 1/2.

These results provide further evidence that TPS yields decoupled pressure solutions at high full-tensor anisotropy, which are not necessarily detected by the flux and resulting flow solution, consistent with decoupling as discussed earlier, the effects are also boundary condition dependent. The results also demonstrate the reliability of FPS with favorable extreme quadrature.

11. Conclusions

New double-families of locally conservative flux-continuous, finite-volume schemes are presented for solving the general-tensor pressure equation on quadrilateral and triangular grids. The new families of schemes have full-pressure continuity imposed across control-volume faces, in contrast to the earlier families of schemes which are pointwise continuous in pressure and flux.

The new families of schemes offer maximum flexibility in range of quadrature and the quadrilateral schemes are exact for piecewise linear and bilinear pressure fields. The double-family of FPS schemes are SPD for a spatially constant full elliptic tensor.

When applying double (and single) family pointwise continuous TPS schemes to full-tensor fields with high anisotropy ratios, the schemes can fail to satisfy the maximum principle, their limited quadrature range lies within a small neighbourhood of the decoupled end point of the quadrature interval, leading to strong spurious oscillations in the solution.

Tensor-coefficient dependent double-family M-matrix limits are derived for locally bounded solutions free of spurious oscillations. This analysis also shows that a consistent locally conservative scheme cannot yield unconditional M-matrices for all tensors. An *optimal support condition* is identified from the M-matrix analysis, via a bounding quadrature point that defines the upper limit on the tensor cross-term. M-matrix analysis of the triangle grid schemes yields essentially the same conditions consistent with optimal support.

For spatially constant tensor coefficients the FPS schemes map on to the CVFE schemes for the entire CVFE quadrature range. In contrast, the pointwise continuous TPS schemes are confined to the neighbourhood of the decoupled quadrature point $\xi = \eta = 1/2$. It is also shown that the fluxes evaluated at $\xi = \eta = 1/2$ do not detect the decoupled solution. A TPS flow result is presented that confirms this observation, while the pressure field suffers from strong spurious oscillations the saturation contours are free of such oscillations, adding further evidence that TPS yields decoupled pressure solutions at high full tensor anisotropy.

The new double-family FPS schemes are tested on problems involving strong full-tensor anisotropy where both M-matrix and monotone matrix conditions are violated. Results for the extended range of quadrature points show that the occurrence of spurious oscillations in the discrete FPS pressure field is minimal. The quadrature points are outside of the neighbourhood of the decoupled zone corresponding to the pointwise continuous TPS schemes.

Quasi-positive QM-matrices are defined for spatially constant tensor fields. The optimal support quadrature points are also shown to be optimal with respect to a QM-matrix. When the tensor is spatially constant, the optimal support quadrature points yield schemes that self-adapt the discretization support locally according to the local orientation of the tensor field. Results show that optimal points yield well resolved solutions that are essentially free of spurious oscillations.

For a variable tensor field a locally upscaled tensor is used to define the tensor dependent optimal quadrature points which are therefore approximate. Alternatively an optimal support scheme is also obtained by anisotropy favoring triangulation, note all triangle grid results have negligible spurious oscillations. However, if the principal direction varies in sign of angle any optimal scheme is dependent on an estimate of the local tensor.

The second strategy presented here exploits the full benefit of the double-family schemes. The notion of extreme anisotropic quadrature is introduced which only depends on the local maximum of the diagonal coefficients of the tensor, and not on the principal direction. The results show that this method yields solutions with resolution that is at least comparable with that of optimal support quadrature. Consequently the extreme quadrature schemes appear advantageous compared to the optimal support schemes due to the independence from the angle of principal anisotropy, which relies on an estimate in the general case.

Acknowledgments

The work of the first author is supported in part by EPSRC Grant GR/S70968/01. The second author would like to thank ExxonMobil Upstream Research Company for supporting this project and permission to publish this work.

Appendix A. Bilinear solution is exact for a poisson equation

We note that $\phi(x,y) = B(x,y)$ identically satisfies the Poisson equation

$$-\int_\Omega \nabla\cdot(\mathbf{K}\nabla\phi)d\tau = -\int_\Omega \nabla\cdot(\mathbf{K}\nabla B)d\tau \tag{46}$$

when B defines the boundary data on ∂_Ω. If $\Omega = \sum_{i=1}^{n}\Omega_i$ and B is a C^0 flux-continuous piecewise bilinear function $B(x,y) = a_i + b_i x + c_i y + d_i xy$, over Ω_i and where $\mathbf{K} = \mathbf{K}_i$, then FPS reproduces exact local outward normal velocities (locally linear in ξ or η) due to use of subcell bilinear basis functions and continuity constraints. If boundary integrals of normal velocity are integrated exactly over the control-volume subfaces FPS is exact and yields the exact solution for Eq. (46). For quadrilateral grids this follows with $\eta = 1/4$, though all quadrature values tested have been found to yield the exact solution within six decimal places. The linear case follows trivially with $d_i = 0$ in the above. In this case FPS is exact forin35(placee1702235

If the tensor is spatially constant then FPS reduces to CVFE over a mesh of constant rectangles or parallelograms. In this case Eq. (46) reduces to the form

$$k_{11}\frac{\partial^2\phi}{\partial x^2}+2k_{12}\frac{\partial^2\phi}{\partial x\partial y}+k_{22}\frac{\partial^2\phi}{\partial y^2}=2k_{12}d \tag{47}$$

and the schemes are exact for ϕ bilinear with $\phi(x,y)=a+bx+cy+dxy$ and ϕ linear with $d=0$.

References

[1] M.G. Edwards, C.F. Rogers, Finite volume discretization with imposed flux continuity for the general tensor pressure equation, Comput. Geo. (2) (1998) 259–290.
[2] M.G. Edwards, Unstructured, control-volume distributed, full-tensor finite volume schemes with flow based grids, Comput. Geo. (6) (2002) 433–452.
[3] M.G. Edwards, Higher-resolution hyperbolic – coupled – elliptic flux-continuous CVD schemes on structured and unstructured grids in 3D, Int. J. Numer. Methods Fluids 51 (2006) 1079–1095.
[4] M. Pal, M.G. Edwards, Quasi-Monotonic Continuous Darcy-Flux Approximation for General 3D Grids of any Element Type Paper SPE 106486, SPE Reservoir Simulation Symposium Houston, Texas, USA, 26–28 February 2007, 14p, doi:10.2118/106486-MS.
[5] M.G. Edwards, M. Pal, Positive definite q-families of continuous subcell Darcy-flux CVD(MPFA) finite-volume schemes and the mixed finite element method, Int. J. Numer. Methods Fluids 57 (2008) 355–387.
[6] I. Aavatsmark, Introduction to multipoint flux approximation for quadrilateral grids, Comput. Geo. (6) (2002) 405–432.
[7] S.H. Lee, P. Jenny, H.A. Tchelepi, A finite-volume method with hexahedral multiblock grids for modeling flow in porous media, Comput. Geo. (6) (2002) 353–379.
[8] S. Verma, Flexible Grids for Reservoir Simulation, Ph.D. Thesis, Stanford University, June 1996.
[9] M.F. Wheeler, I. Yotov, A multipoint flux mixed finite element method, SIAM J. Numer. Anal. 44 (2006) 2082–2106.
[10] R.A. Raviart, J.M. Thomas, A Mixed Finite Element method for Second Order Problems, Lecture Notes in Mathematics, vol. 606, Springer-Verlag, New York, 1977, pp. 292–315.
[11] T.F. Russel, M.F. Wheeler, Finite element and finite difference methods for continuous flows in porous media, in: R.E. Ewing (Ed.), Chapter 2, in the Mathematics of Reservoir Simulation, Frontiers in Applied Mathematics, SIAM, 1983, pp. 35–106.
[12] C.L. Farmer, D.E. Heath, R.O. Moody, A global optimization approach to grid generation, in: Proceedings of the 11th SPE Reservoir Simulation Symposium, Anaheim CA, USA, 17–20 February, 1991, pp. 341–350.
[13] L.J. Durlofsky, A triangle based mixed finite element finite volume technique for modeling two-phase flow through porous media, J. Comput. Phys (1993) 252–266.
[14] T. Arbogast, M.F. Wheeler, I. Yotov, Mixed finite elements for elliptic problems with tensor coefficients as cell centered finite differences, SIAM J. Numer. Anal. 34 (2) (1997) 828.
[15] T.F. Russell, Relationships among some conservative discretization methods, in: Z. Chen et al. (Eds.), Numerical Treatment of Multiphase Flows in Porous Media, Lecture Notes in Physics, vol. 552, Springer, Heidelberg, 2000, pp. 267–282.
[16] J.M. Hyman, M. Shashkov, S. Steinberg, The numerical solution of diffusion problems in strongly heterogeneous non-isotropic materials, J. Comput. Phys. 132 (1997) 130–148.
[17] B. Riviere, Discontinuous Galerkin Method for Solving the Miscible Displacement Problem in Porous Media, Ph.D. Thesis, The University of Texas at Austin, 2000.
[18] B. Riviere, M.F. Wheeler, K. Banas, Discontinuous Glaerkin method applied to a single phase flow in porous media, Comput. Geo. (4) (2000) 337–349.
[19] M.G. Edwards, Symmetric, flux continuous, positive definite approximation of the elliptic full-tensor pressure equation in local conservation form, in: Proceedings of the 13th SPE Reservoir Simulation Symposium, San Antonio, Texas, USA, February 1995, pp. 553–562.
[20] J.M. Nordbotten, I. Aavatsmark, G.T. Eigestad, Monotonicity of control-volume methods, Numerisch 106 (2007) 255–288.
[21] M.J. Mlacnik, L.J. Durlofsky, Unstructured grid optimization for improved monotonicity of discrete solutions of elliptic equations with highly anisotropic coefficients, J. Comput. Phys. 216 (1) (2006) 337–361. 20 July.
[22] M.G. Edwards, H. Zheng, A quasi-positive family of continuous Darcy-flux finite volume schemes with full pressure support, J. Comput. Phys. 227 (2008) 9333–9364.
[23] I. Aavatsmark, G.T. Eigestad, B.T. Mallison, J.M. Nordbotten, A compact multipoint flux approximation method with improved robustness, Numer. Methods Partial Diff. Eqs. 24 (2008) 1329–1360.
[24] M. Pal, M.G. Edwards, Flux-splitting schemes for improved monotonicity of discrete solution of elliptic equation with highly anisotropic coefficients, in: Paper 384, Proceedings, ECCOMAS CFD-2006 Conference, Egmond aan Zee, The Netherlands, 5–8th September, 2006, ISBN:90-9020970-0.
[25] M. Pal, M.G. Edwards, Family of flux-continuous finite-volume schemes with improved monotonicity, in: Paper B009, Proceedings of the 10th European Conference on the Mathematics of Oil Recovery, 4–7th September 2006, ISBN:90-73781-47-7.
[26] C. Le Potier, Schema volume finis pour des operator operateurs de diffusion fortement anisotropes sur des maillages de triangle nonstructures, C.R., Math., Acad. Sci. Paris, Ser. I. 340 (12) (2005) 921–926.
[27] K. Lipnikov, M. Shashkov, D. Svyatskiy, Yu. Vassilevski, Monotone finite volume schemes for diffusion equations on unstructured triangular and shape-regular polygonal meshes, J. Comput. Phys. 227 (2008) 492–512.
[28] M.G. Edwards, M-matrix flux splitting for general full-tensor discretization operators on structured and unstructured grids, J. Comput. Phys. 160 (2000) 1–28.
[29] M.G. Edwards, Symmetric positive definite general tensor discretization operator on unstructured and flow based grids, in: C.L. Farmer, Z.E. Heinemann (Eds.), Paper E04, Proceedings of the Eighth European Conference on Mathematics of Oil Recovery, Freiberg, Germany, 3–6th September, 2002, pp. 22–32, ISBN:90-73781-24-8.
[30] E. Godlewski, P. Raviart, Numerical approximation of hyperbolic systems of conservation laws, App. Math. Sci., vol. 118, Springer-Verlag, New York, 1996.
[31] S. Lamine, M.G. Edwards, Higher order multidimensional wave oriented upwind schemes for flow in porous media on structured and unstructured grids, in: Paper SPE 119187, Proceedings of the Reservoir Simulation Symposium, Houston, Texas, USA, February 2009.
[32] M.G. Edwards, Cross flow, tensors and finite volume approximation with deferred correction, Comput. Methods Appl. Mech. Eng. 151 (1998) 143–161.
[33] M.G. Edwards, Superconvergent renormalization and tensor approximation, in: Proceedings of the Fifth European Conference on the Mathematics of Oil Recovery, Leoben, Austria, 3–6 September 1996, pp. 445–454, ISBN:3-9500542-0-0.
[34] K. Aziz, A. Settari, Petroleum Reservoir Simulation, Applied Science Publishers, London, 1979.